

1
2
3
4
5
6
7
8
9
10
11
12
13
14
15
16
17
18
19
20
21
22
23
24
25

UNIVERSITY OF CALIFORNIA
SANTA CRUZ

**AN INCLUSIVE SEARCH FOR THE DECAY OF A BOOSTED
HIGGS BOSON IN THE $H \rightarrow b\bar{b}$ CHANNEL WITH THE ATLAS
DETECTOR**

A dissertation submitted in partial satisfaction of the
requirements for the degree of
DOCTOR OF PHILOSOPHY

in

PARTICLE PHYSICS

by

Jacob Martin Pasner

October 2019

The Dissertation of Jacob Martin Pasner
is approved:

Professor Jason Nielsen, Chair

Professor Abraham Seiden

Professor Michael Hance

Dean Lori Kletzer
Vice Provost and Dean of Graduate Studies

Copyright © by

Jacob Martin Pasner

2019

31 **Table of Contents**

32	List of Figures	vii
33	List of Tables	xi
34	Abstract	xii
35	Dedication	xiii
36	Acknowledgments	xiv
37	1 Introduction	1
38	I Theoretical Motivations and the Standard Model	2
39	2 The Standard Model and Beyond	3
40	2.1 The Standard Model	4
41	2.1.1 Bosons	5
42	2.1.2 Fermions	8
43	2.2 Quantum Electrodynamics	8
44	2.3 Quantum Chromodynamics	12
45	2.4 The Higgs Mechanism	14

46	2.4.1	Electroweak Symmetry Breaking	14
47	2.4.2	Fermion Mass Terms	18
48	2.4.3	The Higgs Boson	19
49	3	Boosted Higgs at the LHC	21
50	3.1	Higgs Production Mechanisms	22
51	3.2	Parton Distribution Function	25
52	3.3	Branching Ratios	26
53	3.4	Evidence for the SM Higgs	29
54	3.5	Boosted Higgs	32
55	II	Experimental Apparatus and Associated Facilities	35
56	4	The Large Hadron Collider	36
57	4.1	Particle Injection Chain	37
58	4.2	LHC Layout and Design	39
59	4.3	Performance	42
60	4.4	Pile-up at the LHC	44
61	5	The ATLAS Detector	46
62	5.1	ATLAS Coordinate System	49
63	5.2	Tracking with the Inner Detector	53
64	5.2.1	Pixel Detector	55
65	5.2.2	Semiconductor Tracker	55
66	5.2.3	Transition Radiation Tracker	56
67	5.3	Calorimetry	57
68	5.3.1	Electromagnetic Calorimeter	58

69	5.3.2 Hadronic Calorimeter	60
70	5.4 Muon Spectrometer	62
71	III The HbbISR Analysis	65
72	6 Data and Monte-Carlo Simulation	66
73	6.1 Data Used	67
74	6.2 Signal Monte Carlo	67
75	6.3 Background Monte Carlo	68
76	7 Physics Object Selection	69
77	7.1 Calorimeter Jets	70
78	7.2 Track Jets	70
79	7.3 Fat Jets	70
80	7.4 B-tagged Jets	70
81	7.5 Muons	70
82	7.6 Overlap Removal	70
83	8 Event Selection	71
84	8.1 Selected Triggers	71
85	8.2 Pre-selection Studies	71
86	8.3 Signal Selection	71
87	8.4 Optimisation	71
88	9 Background Estimation	72
89	9.1 Multi-jet QCD estimation	72
90	9.2 $t\bar{t}$ control region	72
91	9.3 Single top estimation	72

92	9.4 Hadronic vector boson channel	72
93	10 Systematic Uncertainties	73
94	10.1 Theoretical Uncertainties	73
95	10.2 Experimental Uncertainties	73
96	11 Statistical Fit	74
97	11.1 Profile Likelihood Function	74
98	11.2 Fit Configuration	74
99	11.3 Statistical Tests	74
100	12 Results	75
101	12.1 Expectations	75
102	12.2 Statistical Analysis Results	75
103	12.3 Measurements and Limits	75
104	IV Conclusion	76
105	13 Conclusion	77
106	Bibliography	77
107	A Hadronic Vqq Sherpa Studies	81

108 List of Figures

109	2.1	Summary of several Standard Model total and fiducial production cross	
110		section measurements, corrected for leptonic branching fractions, com-	
111		pared to the corresponding theoretical expectations. All theoretical ex-	
112		pectations were calculated at NLO or higher. The dark-color error bar	
113		represents the statistical uncertainty. The lighter-color error bar repre-	
114		sents the full uncertainty, including systematics and luminosity uncer-	
115		tainties. The data/theory ratio, luminosity used and reference for each	
116		measurement are also shown. Uncertainties for the theoretical predictions	
117		are quoted from the original ATLAS papers. They were not always eval-	
118		uated using the same prescriptions for PDFs and scales. The Wgamma	
119		and Zgamma theoretical cross-sections have non-perturbative corrections	
120		applied to the NNLO fixed order calculations (PRD 87, 112003 (2013)).	
121		Not all measurements are statistically significant yet.	6
122	2.2	Table of all observed fundamental particles of the current Standard Model.	7
123	2.3	A lower dimensionality representation of the shape of the Higgs Potential.	
124		The central peak represents a $v = 0$ rotationally symmetric unstable	
125		state, while the trough represents the infinite choices of minima that can	
126		be selected upon the spontaneous breaking of symmetry.	15
127	3.1	Cross section for the production of the SM Higgs boson as a function of	
128		the center of mass energy (\sqrt{s}) at the LHC. [1]	22
129	3.2	Feynman diagrams representing the dominant Higgs production modes	
130		at the LHC.	23

131	3.3	[2] MMHT2014 NNLO PDFs at $Q^2 = 10\text{GeV}^2$ and $Q^2 = 10^4\text{GeV}^2$ with	
132		associated 68% confidence-level uncertainty bands. The colored regions	
133		indicate the probability of finding the labeled parton with a momentum	
134		fraction given along the x axis. As expected the u_V and d_V contain the	
135		largest fraction of the momentum, however we can also see that many	
136		gluons will exist with smaller fractions of the total momentum. Note	
137		that as Q^2 increases you are more likely to find something besides a u/d	26
138	3.4	Feynman diagrams representing the leading Higgs decay channels. . . .	28
139	3.5	Branching ratios for the decay of the SM Higgs boson near $m_H = 125\text{GeV}$	
140		including theoretical uncertainty bands [1]	29
141	3.6	Best fit values of $\sigma_i \cdot B^f$ for each specific channel $i \rightarrow H \rightarrow f$, as obtained	
142		from the generic parameterisation with 23 parameters for the combina-	
143		tion of the ATLAS and CMS measurements. The error bars indicate the	
144		1σ intervals. The fit results are normalised to the SM predictions for	
145		the various parameters and the shaded bands indicate the theoretical un-	
146		certainties in these predictions. Only 20 parameters are shown because	
147		some are either not measured with a meaningful precision, in the case of	
148		the $H \rightarrow ZZ$ decay channel for the WH , ZH , and $t\bar{t}H$ production pro-	
149		cesses, or not measured at all and therefore fixed to their corresponding	
150		SM predictions, in the case of the $H \rightarrow b\bar{b}$ decay mode for the ggF and	
151		VBF production processes [3].	30
152	3.7	Best fit results for the production signal strengths for the combination of	
153		ATLAS and CMS data. Also shown are the results from each experiment.	
154		The error bars indicate the 1σ (thick lines) and 2σ (thin lines) intervals.	
155		The measurements of the global signal strength μ are also shown [3]. . .	31
156	3.8	Best fit results for the decay signal strengths for the combination of AT-	
157		LAS and CMS data. Also shown are the results from each experiment.	
158		The error bars indicate the 1σ (thick lines) and 2σ (thin lines) intervals [3].	32
159	3.9	Feynman diagram for boosted Higgs decaying to $b\bar{b}$	33
160	3.10	Cartoon showing columnated Higgs and ISR as a result of the large boost	
161		due to their mutual recoil.	34
162	4.1	CERN accelerator complex	38
163	4.2	Labeled diagram of all the experiments at the LHC indicating the counter	
164		circulating beams and points of interest along the circumference of the	
165		accelerator.	40

166	4.3	Depiction of a LHC dipole magnet 2-in-1 design labeling the major components	41
167			
168	4.4	Luminosity is monitored as both a running total known as the Integrated Luminosity as depicted in (a) and as an instantaneous quantity as shown in (b).	44
169			
170			
171	4.5	Pileup for data taking periods 2015 - 2018	45
172	5.1	[10] Here we see a cut-away side view of the ATLAS detector with the major components labeled. Note that within each of these labeled components there may exist multiple different detector technologies. For scale two people in red are shown standing between the disk muon chambers on the left side of the figure.	47
173			
174			
175			
176			
177	5.2	This slice of the ATLAS detector depicts how different particles interact with each component of the detector it crosses. A dashed line indicates no interaction while a solid line indicates interaction. Electrons (yellow/green) and charged hadrons (red) interact with the tracker and curve in the solenoid's magnetic field. Electrons and photons (yellow/green) are absorbed by the Electromagnetic calorimeter. All hadrons (red/yellow) are absorbed by the Hadronic calorimeter. The muons (orange) curve in both the solenoid and toroid magnetic fields before exiting the detector. Finally, the neutrinos (white) pass through the entire detector without interacting.	50
178			
179			
180			
181			
182			
183			
184			
185			
186			
187	5.3	[11] A cartoon view of the the LHC from above showing the SPS, LHC and the four main experiments of the LHC: ATLAS, CMS, LHCb, and ALICE. The standard cartesian coordinate system is shown with its origin at the ATLAS interaction point, the positive x -axis towards the center of the LHC, the positive y -axis pointing upwards, and the positive z -axis pointing along the beamline towards the "A-side"	51
188			
189			
190			
191			
192			
193	5.4	Modified from [11] this cartoon represents a selection of pseudorapidity (η) values overlaid with some cartesian coordinates (dashed black lines). The red lines are drawn for $\eta = \pm 0.5, 1.0, 3.0$	52
194			
195			
196	5.5	[12] Diagram of inner detector	53
197	5.6	[15] Schematic of the Inner Detector including η lines. Each component shown is cylindrically symmetric leading to a multi-layered detector. . .	54
198			
199	5.7	[10] A cutaway diagram of ATLAS sampling calorimeters	57

200	5.8	[10] Sketch of LAr EMC barrel module where the lead and liquid ar-	
201		gon layers are visible in an accordion like geometry. Looking from the	
202		foreground to the back there are 3 different types of cells visible.	59
203	5.9	[10] Schematic of a tile calorimeter module including a depiction of the	
204		connection between the scintillator tile to the photomultiplier via a wavelength-	
205		shifting fibre.	61
206	5.10	[10] A cut-away diagram of the ATLAS muon system and its many sub-	
207		detectors.	63

208 List of Tables

209	3.1	SM Higgs boson production cross sections in units of pb for $m_H =$	
210		125 GeV in pp collisions as a function of the center-of-mass energy, \sqrt{s} ,	
211		at the LHC. The predictions for the ggF channel include the latest N3LO	
212		results leading to reduced theoretical uncertainties by a factor around 2	
213		compared to the N2LO results [1].	24
214	3.2	The branching ratios and the relative uncertainty for a Standard Model	
215		Higgs boson with $m_H = 125$ GeV [1].	27

Abstract

An Inclusive Search for the decay of a Boosted Higgs boson in the $H \rightarrow b\bar{b}$

channel with the ATLAS detector

by

Jacob Martin Pasner

Abstract placeholder

222

Dedication

223

Dedication

224

Dedication

Acknowledgments

226 **Chapter 1**

227 **Introduction**

228 Every dissertation should have an introduction. You might not realize it, but the
229 introduction should introduce the concepts, backgrouand, and goals of the dissertation.

230

Part I

231

Theoretical Motivations and the

232

Standard Model

Chapter 2

The Standard Model and Beyond

The Standard Model (SM) of Particle Physics is humanities best "guess" at the force laws that describe the observed behavior of all particles in our universe. Its formulation is a collection of Quantum Field Theories (QFT) that describe the following interactions of elementary matter in Nature: the electromagnetic force, the weak nuclear force and the strong nuclear force. Gravity is noticeably absent as currently there is no viable quantum theory for observed gravitational effects. The Glashow-Salam-Weinberg (GSW) theory of Quantum Electrodynamics (QED) describes the electromagnetic and weak forces, while Quantum Chromodynamics (QCD) describes the strong force. These theories form the following symmetry group of the Standard Model.

$$\underbrace{\mathrm{SU}_C(3)}_{\mathrm{QCD}} \otimes \underbrace{\mathrm{SU}_L(2) \otimes \mathrm{U}_Y(1)}_{\mathrm{GSW}}. \quad (2.1)$$

244 The gauge principle states that the SM Lagrangian and its predictions must be invariant
245 under local transformations using an operator from any of these constituent groups.
246 Thus, any theory must only include transformations and terms that maintain the local
247 invariance of the complete Lagrangian. In particular, this requirement was violated
248 by any attempt to include an explicit mass term for the Gauge Bosons of QED and
249 for all fermions. Around 1960 a possible solution to this lack of mass was proposed
250 in the form of the spontaneous breaking of the ElectroWeak symmetry, now known as
251 the Higgs mechanism. In the following sections I will go into more detail about the
252 Lagrangian formalism of the Standard Model, QCD, QED and this recently verified
253 Higgs Mechanism.

254 **2.1 The Standard Model**

255 At the turn of the 20th century our understanding of the constituent matter of the uni-
256 verse was limited to what we could see with microscopes and imply from the observations
257 of light and electricity, giving us evidence for both the photon and the electron. In the
258 first half of the century we discovered the field of subatomic physics with Rutherford's
259 1911 gold foil scattering experiment, and Dirac successfully demonstrated the quantiza-
260 tion of the electromagnetic field, the first step towards a fully Gauge Invariant Quantum
261 Field Theory. In the second half we literally delved deeper, discovering that the nucleus
262 contained structure and extended our theories to include the the complex mechanics of
263 quarks and gluons. With the discovery of the Higgs in 2013 the Standard Model has

264 become an irrefutable framework as can be seen in the high level of agreement between
265 theory and experiment in Figure 2.1.

266 The QCD and QED theories predict two classes of particles: fermions and bosons shown
267 in Figure 2.2. These particles represent the quanta of the quantum fields of the Standard
268 Model and the mediators of the fundamental forces of Nature.

269 2.1.1 Bosons

270 These spin-1 particles are known as the vector gauge bosons and are the force carriers
271 of the SM. The most commonly known is the electromagnetic force's un-charged and
272 massless photon (γ) which interacts with all charged particles and is often referred to
273 as "light". The weak nuclear force is involved in nuclear interactions such as beta
274 decays and is carried by 3 bosons all of which have mass and couple to all fermions;
275 the W^\pm bosons, which mediate the charged weak nuclear interaction and allow for
276 flavor changing currents; and the Z boson which mediates the neutral weak nuclear
277 interaction. Finally we have 8 massless gluons which mediate the strong nuclear force
278 and only interact with fermions with a "color" charge such as the quarks contained
279 inside the nucleus. The only spin-0 boson, the Higgs Boson (h) is the key to generating
280 mass terms in the SM Lagrangian for the massive Gauge Bosons and for fermions.
281 This is done through the so called Higgs Mechanism and is discussed in more detail in
282 Section 2.4.

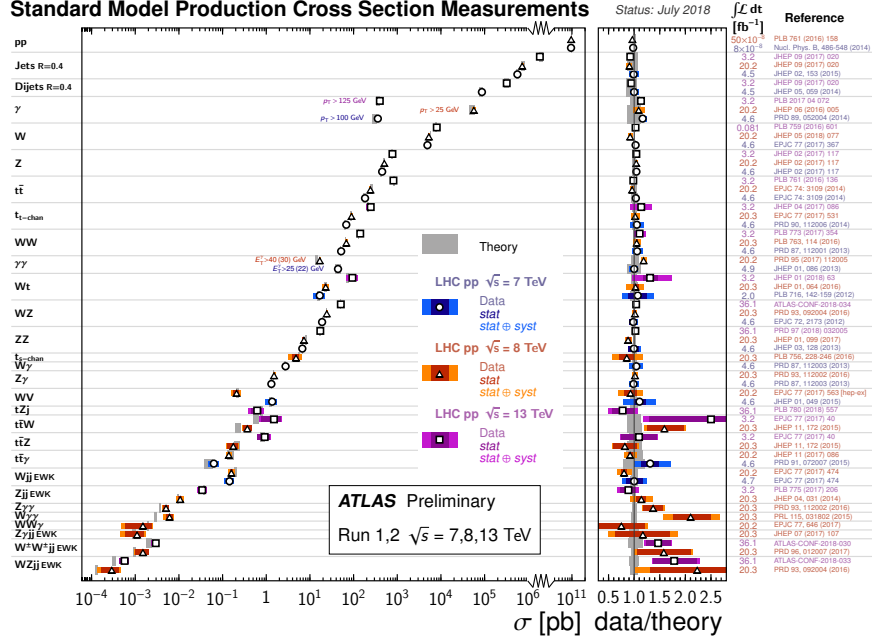


Figure 2.1: Summary of several Standard Model total and fiducial production cross section measurements, corrected for leptonic branching fractions, compared to the corresponding theoretical expectations. All theoretical expectations were calculated at NLO or higher. The dark-color error bar represents the statistical uncertainty. The lighter-color error bar represents the full uncertainty, including systematics and luminosity uncertainties. The data/theory ratio, luminosity used and reference for each measurement are also shown. Uncertainties for the theoretical predictions are quoted from the original ATLAS papers. They were not always evaluated using the same prescriptions for PDFs and scales. The $W\gamma$ and $Z\gamma$ theoretical cross-sections have non-perturbative corrections applied to the NNLO fixed order calculations (PRD 87, 112003 (2013)). Not all measurements are statistically significant yet.

Standard Model of Elementary Particles


















three generations of matter (fermions)						interactions / force carriers (bosons)	
	I	II	III				
mass	$\approx 2.2 \text{ MeV}/c^2$	$\approx 1.28 \text{ GeV}/c^2$	$\approx 173.1 \text{ GeV}/c^2$	0	$\approx 124.97 \text{ GeV}/c^2$		
charge	$\frac{2}{3}$	$\frac{2}{3}$	$\frac{2}{3}$	0	0		
spin	$\frac{1}{2}$	$\frac{1}{2}$	$\frac{1}{2}$	1	0		
QUARKS	 u up	 c charm	 t top	 g gluon	 H higgs		
	 d down	 s strange	 b bottom	 γ photon		SCALAR BOSONS	
	 e electron	 μ muon	 τ tau	 Z Z boson			
LEPTONS	 ν_e electron neutrino	 ν_μ muon neutrino	 ν_τ tau neutrino	 W W boson			
	$\approx 0.511 \text{ MeV}/c^2$ -1 $\frac{1}{2}$	$\approx 105.66 \text{ MeV}/c^2$ -1 $\frac{1}{2}$	$\approx 1.7768 \text{ GeV}/c^2$ -1 $\frac{1}{2}$	$\approx 91.19 \text{ GeV}/c^2$ 0 1	$\approx 80.39 \text{ GeV}/c^2$ ± 1 1	GAUGE BOSONS VECTOR BOSONS	

Figure 2.2: Table of all observed fundamental particles of the current Standard Model.

2.1.2 Fermions

These spin-1/2 particles can be further broken up into two distinct families of particles, the leptons and the quarks, both of which contain three "generations" each with an "up" and "down" type particle. The leptons "up" type members are the electrically charged electron (e), muon (μ) and tau (τ) while the "down" type are their electrically neutral counterparts ν_e , ν_μ , ν_τ . The quarks "up" type members are the up (u), charm (c), and top (t) each with a $+2/3$ elementary charge, while the "down" type members are the down (d), strange (s), and bottom (b) all of which have a $-1/3$ elementary charge. Each quark carries a "color" charge thus allowing them to participate in strong force interactions. Due to the observed color confinement of the strong force these quarks are only observed in colorless bound states known as "mesons" (1 quark and 1 anti-quark) and "baryons" (an odd number of quarks and anti-quarks). All of the above fermions have an anti-particle partner which has the opposite electrical charge but is otherwise identical.

2.2 Quantum Electrodynamics

In the SM the Electromagnetic and Weak nuclear forces are unified into the Electroweak interaction which is represented by the $SU(2)_L \times U(1)_Y$ gauge group. The L represents the physical observable that the Weak interaction, and thus the $SU(2)$ transformation, only acts on left handed particle states. The Y states that this is the $U(1)$ symmetry

for the weak hypercharge Y instead of the electromagnetic charge. The particle states for these interactions are solutions to the Dirac equation and are represented as Dirac spinor doublets (Ψ_L) for the left handed states, and as Dirac spinor singlets (Ψ_R) for the right handed states. Thus when a general transformation from the Electroweak gauge group is applied to the left handed spinor doublet you get Equation (2.2)

$$\Psi_L \rightarrow \Psi'_L = \exp \left(\underbrace{ig' \frac{Y_L}{2} \zeta(x)}_{U(1)_Y} + \underbrace{ig_W \boldsymbol{\alpha}(x) \cdot \mathbf{T}}_{SU(2)_L} \right) \Psi_L. \quad (2.2)$$

For the right handed spinor singlet the $SU(2)_L$ doesn't contribute and you get Equation (2.3)

$$\Psi_R \rightarrow \Psi'_R = \exp \left(\underbrace{ig' \frac{Y_R}{2} \zeta(x)}_{U(1)_Y} \right) \Psi_R. \quad (2.3)$$

We can see that these local gauge transformations have introduced space-time dependent terms $\boldsymbol{\alpha}(x)$ and $\zeta(x)$ into our electroweak Lagrangian. Due to the derivatives contained within the kinetic term of this lagrangian, this new configuration would introduce additional terms, thus violating our required local gauge invariance. Luckily, we can remove these additional terms by replacing the standard derivative (∂_μ) with the covariant derivative (D_μ) as seen in Equation (2.4) for the left handed states and Equation (2.5) for the right handed states.

$$D_\mu = \partial_\mu - \underbrace{\frac{1}{2}ig' B_\mu Y_L}_{U(1)_Y} - \underbrace{\frac{1}{2}ig_W \mathbf{W}_\mu \cdot \boldsymbol{\tau}}_{SU(2)_L} \quad (2.4)$$

$$D_\mu = \partial_\mu - \underbrace{\frac{1}{2}ig' B_\mu Y_R}_{U(1)_Y} \quad (2.5)$$

316 Here we see two new gauge fields; B_μ the weak hypercharge field and \mathbf{W}_μ the charged
 317 weak field as well as the associated coupling constants g', g_W, Y_L, Y_R and the $SU(2)$
 318 generators $\boldsymbol{\tau}$. Next we write down the transformation properties of these new fields

$$\mathbf{W}_\mu(x) \rightarrow \mathbf{W}'_\mu(x) = \mathbf{W}_\mu + \partial_\mu \boldsymbol{\alpha}(x) + g_W \mathbf{W}_\mu(x) \times \boldsymbol{\alpha}(x) \quad (2.6)$$

$$B_\mu \rightarrow B'_\mu = B_\mu + \frac{1}{g'} \partial_\mu \zeta(x) \quad (2.7)$$

319 The form of these fields is chosen such that the final Lagrangian is invariant under
 320 $SU(2)_L \times U(1)_Y$ transformations, and thus we have restored gauge invariance for the
 321 kinetic term of our electroweak Lagrangian! Inserting these new definitions into the
 322 Lagrangian for the spinor field Ψ which satisfies the free-particle Dirac equation we get

$$\mathcal{L} = i\bar{\Psi}_L \gamma^\mu \left(\partial_\mu - \frac{1}{2}ig' B_\mu Y_L - \frac{1}{2}ig_W \mathbf{W}_\mu \cdot \boldsymbol{\tau} \right) \Psi_L + i\bar{\Phi}_R \gamma^\mu \left(\partial_\mu - \frac{1}{2}ig' B_\mu Y_R \right) \Phi_R \quad (2.8)$$

323 Next we must construct the gauge field self interaction and mass terms

$$\mathcal{L} = -\frac{1}{4}\mathbf{F}_{\mu\nu}\mathbf{F}^{\mu\nu} - \frac{1}{4}B_{\mu\nu}B^{\mu\nu} + \frac{1}{2}M_W^2\mathbf{W}_\mu\mathbf{W}^\mu + \frac{1}{2}M_B^2B_\mu B^\mu \quad (2.9)$$

324 where the field tensors $\mathbf{F}^{\mu\nu}$ and $B^{\mu\nu}$ are defined to be

$$\mathbf{F}^{\mu\nu} = \partial^\mu\mathbf{W}^\nu - \partial^\nu\mathbf{W}^\mu + g\mathbf{W}^\mu \times \mathbf{W}^\nu \quad (2.10)$$

$$B^{\mu\nu} = \partial^\mu B^\nu - \partial^\nu B^\mu \quad (2.11)$$

325 The field tensor terms in Equation (2.9) are invariant under our gauge transformations,
 326 but simply plugging in Equation (2.4) or Equation (2.5) into the mass terms shows
 327 that these terms violate gauge invariance thus implying $M_W = 0$ and $M_B = 0$ in direct
 328 contradiction of the observed masses of the weak gauge bosons. This issue arises again
 329 for fermion mass terms as illustrated below for the electron field (e) expanded in its chiral
 330 basis.

$$m_e\bar{e}e = m_e \begin{pmatrix} e_R^\dagger & e_L^\dagger \end{pmatrix} \begin{pmatrix} e_L \\ e_R \end{pmatrix} = m_e(e_R^\dagger e_L + e_L^\dagger e_R) \quad (2.12)$$

331 Remembering that the left and right handed spinors of the electroweak interaction trans-
 332 form differently we see that this mixture of right and left fields violates gauge invariance.
 333 This again forces us to conclude that $m_e = 0$ in contradiction to the observation that

the electron does indeed have mass. As mentioned in Section 2.1.1 the resolution to these mass mysteries lies in the Higgs mechanism discussed in Section 2.4

2.3 Quantum Chromodynamics

Quantum Chromodynamics is the continuation of the mathematical framework established by Quantum Electrodynamics (Section 2.2, this time for the strong force described by the $SU(3)_C$ gauge group where the C represents the "color" charge of QCD. This color charge doesn't imply actual visible color, but is useful as an analogy to the visible spectrum where a combination of red, green, and blue generates white. For QCD the combination of red, green, and blue color charges results in a colorless object. As mentioned in Section 2.1.2 the quarks will contain a color (anti-color) charge represented by a color triplet field which transforms under the general $SU(3)$ transformation as shown here

$$q = \begin{pmatrix} q_r \\ q_g \\ q_b \end{pmatrix} \rightarrow q' = \exp \left(ig_s \sum_{k=1}^8 \eta_k(x) \frac{\lambda_k}{2} \right) q \quad (2.13)$$

Here the λ_k are the generators for $SU(3)$, $\eta(x)_k$ is the space-time dependancy for each generator, and g_s is the strong coupling constant. As with QED, the introduction of these space-time dependant terms introduces new terms into the kinematic portion of

the lagrangian thus spoiling our gauge invariance. Again, we introduce a covariant derivative to restore invariance

$$D_\mu = \partial_\mu - ig_s G_\mu^k \frac{\lambda_k}{2} \quad (2.14)$$

Here the G_μ^k are the new fields introduced for the 8 gluons. These new fields transform under $SU(3)$ as shown in Equation (2.15)

$$G_\mu^k \rightarrow G'^k_\mu = G_\mu^k + \partial_\mu \eta_k(x) + g_s f_{klm} \eta_l(x) G_\mu^m \quad (2.15)$$

Given these definitions we can construct the QCD Lagrangian (\mathcal{L}_{QCD}) as shown in Equation (2.16) where the gluon field tensor $G_k^{\mu\nu}$ is the one defined in Equation (2.17)

$$\mathcal{L}_{QCD} = \bar{q}(i\gamma_\mu D^\mu - m_q)q - \frac{1}{4} G_k^{\mu\nu} G_{k\mu\nu} \quad (2.16)$$

$$G_k^{\mu\nu} = \partial^\mu G_k^\nu - \partial^\nu G_k^\mu + g_s f_{klm} G^\mu G_m^\nu \quad (2.17)$$

The strong force is peculiar in that we experimentally observe only colorless objects in the form of bound states of quarks known as hadrons. Qualitatively, when a bound state of quarks (meson or baryon) is given sufficient energy to separate the strong force dramatically increases in strength. At the point where the objects would separate, and

359 thus no longer be colorless, it becomes energetically favorable to produce a quark/anti-
 360 quark pair in a process known as hadronization. In other words, attempting to separate
 361 a bound quark state into its colored constituents simply results in new colorless bound
 362 states. This requirement of colorless objects by the strong force is known as color
 363 confinement. For highly energetic strong interactions at hadron colliders the result is
 364 an expanding chain of hadronizing quarks and gluons and their decay products known
 365 as a jet.

366 **2.4 The Higgs Mechanism**

367 The Higgs Mechanism is the system by which the gauge bosons and fermions attain mass
 368 through the spontaneous breaking of the electroweak symmetry of the Higgs potential.
 369 This section will also discuss briefly the couplings of the Higgs boson to massive particles,
 370 as well as it's self couplings.

371 **2.4.1 Electroweak Symmetry Breaking**

372 The Higgs field is expressed as a complex doublet, Φ , and thus has four components as
 373 shown in Equation (2.18)

$$\Phi(x) = \begin{pmatrix} \phi^+ \\ \phi^0 \end{pmatrix} = \frac{1}{\sqrt{2}} \begin{pmatrix} \phi_1(x) + i\phi_2(x) \\ \phi_3(x) + i\phi_4(x) \end{pmatrix} \quad (2.18)$$

374 The four components of this field each represent a degree of freedom which will be
 375 used to give the longitudinal polarizations of the gauge bosons W^\pm, Z and the mass of
 376 the Higgs boson. The resulting lagrangian for the higgs includes a kinetic term (K) as
 377 well as the Higgs potential (V) all of which are invariant under the Electroweak gauge
 378 symmetry $SU(2)_L \times U(1)_Y$

$$\mathcal{L}_{\text{Higgs}} = \underbrace{(D_\mu \Phi)^\dagger D^\mu \Phi}_{\text{K}} - \underbrace{(\mu^2 \Phi^\dagger \Phi + \lambda (\Phi^\dagger \Phi)^2)}_{\text{V}} \quad (2.19)$$

379 Here we constrain $\mu^2 < 0$ and $\lambda > 0$ such that the potential forms a stable minima. The
 380 shape of this potential is shown in Figure 2.3 and is often referred to as the "Mexican-hat"
 381 or "Wine-bottle" potential.

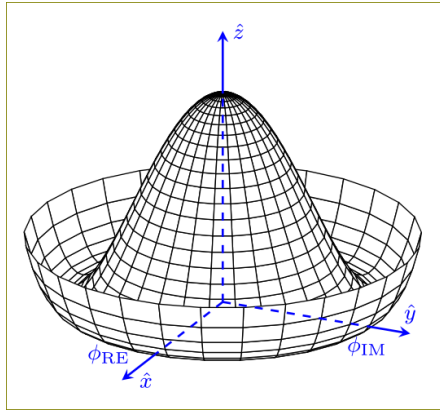


Figure 2.3: A lower dimensionality representation of the shape of the Higgs Potential. The central peak represents a $v = 0$ rotationally symmetric unstable state, while the trough represents the infinite choices of minima that can be selected upon the spontaneous breaking of symmetry.

382 Whatever you call it, this potential is significant in that its minimum is not at $\Phi = 0$
 383 but instead is symmetric around the origin thus defining an infinite number of states
 384 that minimize V . The value of this minima can be calculated by taking the derivative
 385 of V with respect to Φ and setting it equal to 0. This value, also known as the vacuum
 386 expectation value (vev) has been found to be $v \equiv \sqrt{-\mu^2/\lambda} = 246$ GeV. In order to reach
 387 this ground state energy, the Higgs field must spontaneously break this symmetry, and
 388 thus acquire an arbitrary single value. For ease of calculation we orient our coordinate
 389 system such that

$$\langle \Phi(x) \rangle = \frac{1}{\sqrt{2}} \begin{pmatrix} 0 \\ v \end{pmatrix} \quad (2.20)$$

390 Next we parameterize small perturbations around the minimum of the Higgs potential
 391 as

$$\langle \Phi(x) \rangle = \frac{1}{\sqrt{2}} \begin{pmatrix} 0 \\ v + h(x) \end{pmatrix} \exp \left(i \frac{\tau^i}{2} \theta^i(x) \right) \quad (2.21)$$

392 Here the real scalar field $h(x)$ corresponds to radial perturbations of the minima and
 393 while the three $\theta^i(x)$ are the Nambu-Goldstone fields with values determined by your
 394 choice of gauge. Choosing the unitary gauge of $\theta^i(x) = 0$ and expanding the kinetic

395 term of Equation (2.19) around the vev we get

$$\mathcal{L}_{\text{Higgs},K} = \frac{g^2 v^2}{8} \left((W_\mu^-)^\dagger W^{-\mu} + (W_\mu^+)^\dagger W^{+\mu} \right) + \frac{1}{2} \begin{pmatrix} W_\mu^{3\dagger} & B_\mu^\dagger \end{pmatrix} \mathbf{M}^2 \begin{pmatrix} W^{3\mu} \\ B^\mu \end{pmatrix} + \dots \quad (2.22)$$

396 Here the first term is the physical mass term for the W^\pm bosons where we have con-
 397 structed their charge eigenstates out of the $W^{1,2}$ fields like this $W^\pm = \frac{1}{\sqrt{2}}(W^1 \mp iW^2)$.
 398 The second term represents the mixture of the W^3 and B fields through the mass ma-
 399 trix \mathbf{M} . By diagonalizing this matrix and identifying the mass eigenstates we find the
 400 physical fields of the photon (γ) and the Z boson

$$\mathbf{M}_{\text{Diagonalized}}^2 = \begin{pmatrix} 0 & 0 \\ 0 & \frac{v^2}{4}(g_W^2 + g'^2) \end{pmatrix} \quad (2.23)$$

401 The upper left diagonal element corresponds to the massless photon while the lower
 402 right diagonal element gives the mass of the massive Z boson. This leaves us with the
 403 following masses for the 4 Electroweak bosons

$$m_W = \frac{1}{2} g_W v \quad , \quad m_Z = \frac{1}{2} v \sqrt{g_W^2 + g'^2} \quad , \quad m_\gamma = 0 \quad (2.24)$$

404 The masses of the W^\pm and Z gauge bosons can be related through the Weinberg angle

405 or mixing angle which

$$\theta_W = \cos^{-1} \left(\frac{g_W}{\sqrt{g_W^2 + g'^2}} \right) \rightarrow m_Z = \frac{m_W}{\cos \theta_W} \quad (2.25)$$

406 Using this definition we can write out the exact mixture of B and W^3 that make up the
407 photon and Z boson

$$\gamma = \cos(\theta_W)B + \sin(\theta_W)W^3 \quad (2.26)$$

$$Z = -\sin(\theta_W)B + \cos(\theta_W)W^3 \quad (2.27)$$

408 2.4.2 Fermion Mass Terms

409 In Section 2.2 we saw that fermion mass terms violate gauge invariance due to the
410 mixing of the left and right chiral states. The Higgs mechanism again allows for a gauge
411 invariant method of generating mass terms but this time through the Yukawa coupling
412 of the Higgs field to the fermion fields. To see an example of this here is the Yukawa
413 coupling term for the electron doublet (Ψ_L) and singlet (Ψ_R) coupling to the Higgs field
414 (Φ) after spontaneous symmetry breaking giving it the form shown in Equation (2.21)
415 where we have again choosen the unitary gauge $\Phi^i(x) = 0$.

$$\mathcal{L}_{Yukawa} = -g_e \left[\bar{\Psi}_L \Phi \Psi_R + \bar{\Psi}_R \Phi^\dagger \Psi_L \right] \quad (2.28)$$

$$= -\frac{g_e}{\sqrt{2}} \left[\begin{pmatrix} \bar{\nu}_e & \bar{e} \end{pmatrix}_L \begin{pmatrix} 0 \\ \nu + h \end{pmatrix} e_R + \bar{e}_R \begin{pmatrix} 0 & (\nu + h) \end{pmatrix} \begin{pmatrix} \nu_e \\ e \end{pmatrix}_L \right] \quad (2.29)$$

$$= -\underbrace{\frac{g_e}{\sqrt{2}} \nu}_{m_e} (\bar{e}_L e_R + \bar{e}_R e_L) - \underbrace{\frac{g_e}{\sqrt{2}} h}_{g_{e,h}} (\bar{e}_L e_R + \bar{e}_R e_L) \quad (2.30)$$

416 And voila, we have successfully generated mass terms for our fermion field and main-
 417 tained the gauge invariance of our Lagrangian by using all gauge invariant fields. This
 418 operation has also left us with the second term which represents the coupling of the
 419 electron to the higgs itself thus giving us the form of it's coupling constant $g_{e,h}$. Using
 420 our newly found mass of the electron m_e we can write

$$g_{e,h} = \frac{g_e}{\sqrt{2}} = \frac{m_e}{\nu} \quad (2.31)$$

421 Thus we see that the coupling of the higgs boson to a fermion is indeed proportional to
 422 the mass of the fermion itself. In other words, the more massive a particle is, the more
 423 the higgs couples to it and vice versa.

424 2.4.3 The Higgs Boson

425 As we have seen this Higgs mechanism not only properly mixes the gauge fields thus
 426 providing them gauge invariant mass terms, it also properly combines the left and right

427 chiral states of fermions to produce their mass terms. The final step then is to determine
 428 an observable of the theory that can be tested in experiment, namely the existence of a
 429 massive scalar particle, the Higgs boson itself.

430 Turning our attention to the potential term (V) of Equation (2.19) and substituting in
 431 our definition for Φ given in Equation (2.21) we find

$$\mathcal{L}_{\text{Higgs,V}} = \frac{1}{2}\mu^2\nu^2 - \mu^2h^2 + \lambda\nu h^3 + \frac{1}{4}\lambda h^4 \quad (2.32)$$

432 Here the first term is constant and thus can be ignored. The second term is the mass
 433 term for the SM particle the Higgs boson, $m_h = \sqrt{-2\mu^2} = \sqrt{2\lambda}\nu$. Remembering that
 434 $h = h(x)$ was used for small radial perturbations of the Higgs field we can identify the
 435 Higgs boson simply as an excitation of the Higgs field. Finally, the third and fourth
 436 terms represent the Higgs boson self-couplings. With these couplings and mass terms
 437 in hand we can now move on to the experimental verification of this theory as discussed
 438 next in Chapter 3.

Chapter 3

Boosted Higgs at the LHC

In Chapter 2 I've shown how the higgs mechanism resolves inconsistencies of the model surrounding the generation of gauge boson and fermion mass terms while also maintaining gauge invariance. However to understand the search for and resulting discovery of this SM Higgs boson requires the discussion of how one goes about producing and detecting the physical object itself. In order to gather sufficient statistics to validate the theory we require a collider capable of putting enough energy into a collision to rapidly produce Higgs bosons for study. To this end the Large Hadron Collider (LHC) discussed in Chapter 4 was laboriously designed, funded, and constructed by the largest international collaboration of scientists on the planet. In this chapter I will discuss the relevant Higgs boson production mechanisms available at the LHC as well as the various decay modes of the Higgs that were used for its discovery, and are currently used to measure its properties.

3.1 Higgs Production Mechanisms

At the LHC the dominate production mechanisms for the higgs in order of decreasing cross section are: gluon-fluon fusion (ggF), vector boson fusion (VBF), vector boson associated production or “Higgsstrahlung” (VH), and associated production with $t\bar{t}$ ($t\bar{t}H$) and $b\bar{b}$ ($b\bar{b}H$). The cross sections with associated theoretical uncertainties for each is shown as a function of the center of mass energy \sqrt{s} in Figure 3.1 and the actual feynman diagrams can be seen in Figure 3.2. For reference the exact produciton cross sections for a variety of center of mass energies are detailed in Table 3.1.

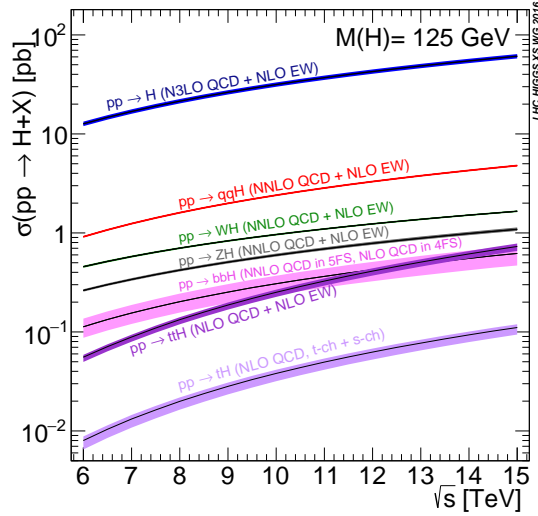


Figure 3.1: Cross section for the production of the SM Higgs boson as a function of the center of mass energy (\sqrt{s}) at the LHC. [1]

The dominant Higgs production mechanism at hadron colliders is ggF. This may seem strange as gluons are massless and thus do not couple directly to the Higgs. Instead the

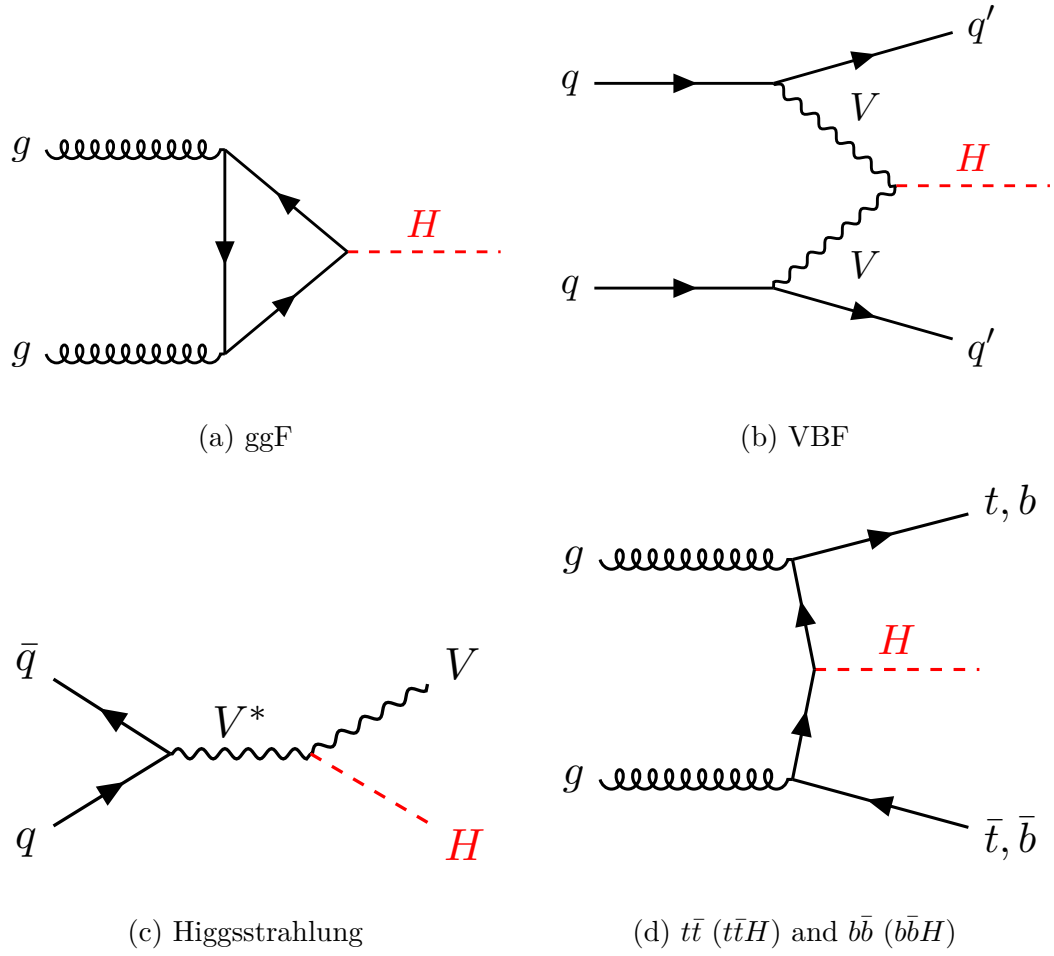


Figure 3.2: Feynman diagrams representing the dominant Higgs production modes at the LHC.

Table 3.1: SM Higgs boson production cross sections in units of pb for $m_H = 125$ GeV in pp collisions as a function of the center-of-mass energy, \sqrt{s} , at the LHC. The predictions for the ggF channel include the latest N3LO results leading to reduced theoretical uncertainties by a factor around 2 compared to the N2LO results [1].

\sqrt{s} (TeV)	ggF	VBF	WH	ZH	$t\bar{t}H$	Total (pb)
8	$21.4^{+5\%}_{-5\%}$	$1.60^{+2\%}_{-2\%}$	$0.70^{+3\%}_{-3\%}$	$0.42^{+5\%}_{-5\%}$	$0.13^{+8\%}_{-13\%}$	24.2
13	$48.6^{+5\%}_{-5\%}$	$3.78^{+2\%}_{-2\%}$	$1.37^{+2\%}_{-2\%}$	$0.88^{+5\%}_{-5\%}$	$0.50^{+9\%}_{-13\%}$	55.1
14	$54.7^{+5\%}_{-5\%}$	$4.28^{+2\%}_{-2\%}$	$1.51^{+2\%}_{-2\%}$	$0.99^{+5\%}_{-5\%}$	$0.60^{+9\%}_{-13\%}$	62.1

463 gluons indirectly couple to the Higgs via a quark loop. As discussed in Section 2.4.2,
464 the coupling of a fermion is proportional to m_f so the dominant contribution to this
465 quark loop comes from the top quark.

466 The second largest cross section for Higgs production at the LHC comes from the VBF
467 mechanism. In VBF the initial state quarks scatter via the exchange of a W^\pm or
468 Z boson which subsequently radiates the Higgs boson. Unlike ggF this production
469 mechanism scatters the initial state quarks which allows them to be observed as part of
470 the interaction. The existence of these extra quarks makes these interactions easier to
471 select for during analysis.

472 Next we have Higgs production in association with a vector boson. The cross section for
473 this is even lower than the above two, but remains important due to the easily selected
474 signature of the decaying vector boson. The largest background at the LHC is multijet
475 events coming from interactions that produce strong force objects. Thus the leptons

476 from the boson's decay act as a discriminator from this multijet background greatly
477 reducing its effect on sensitivity.

478 With the lowest cross section of the four methods discussed we have the production of
479 the Higgs in association with either $b\bar{b}$ or $t\bar{t}$. This channel is important due to our
480 ability to measure not only the Higgs, but also the quarks that it directly coupled with.
481 This allows us to directly measure the coupling of the Higgs to that quark, unlike the
482 ggF method where the quark in the loop is never directly observed.

483 As we can see, each of these methods has its advantages and disadvantages as well as
484 different valuable information that can be extracted. The result is a need for many
485 different analysis using different techniques to search for each mechanism.

486 3.2 Parton Distribution Function

487 The LHC collides protons, however looking at the feynman diagrams in Figure 3.2
488 we see that it is quarks and gluons (a.k.a partons) that produce these fundamental
489 interactions. This is an indicator that when we calculate the production cross section
490 for a process at the LHC, we have to not only consider the hard-scatter probability of
491 the specific diagram, but also consider the composition of the proton itself. Specifically,
492 we must consider the fraction of the total momentum of the proton held by each of
493 its constituent partons. This concept is described by Parton Distribution Functions
494 (PDFs) which give the probability that the indicated parton carries momentum fraction

495 x of the proton when probed at with energy scale Q . An example PDF for $Q = 10\text{GeV}^2$
 496 and $Q = 10^4\text{GeV}^2$ in Figure 3.3

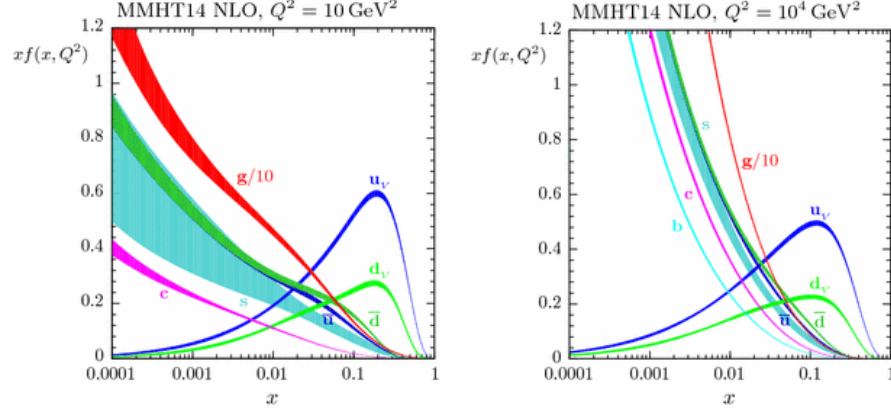


Figure 3.3: [2] MMHT2014 NNLO PDFs at $Q^2 = 10\text{GeV}^2$ and $Q^2 = 10^4\text{GeV}^2$ with associated 68% confidence-level uncertainty bands. The colored regions indicate the probability of finding the labeled parton with a momentum fraction given along the x axis. As expected the u_V and d_V contain the largest fraction of the momentum, however we can also see that many gluons will exist with smaller fractions of the total momentum. Note that as Q^2 increases you are more likely to find something besides a u/d

497 3.3 Branching Ratios

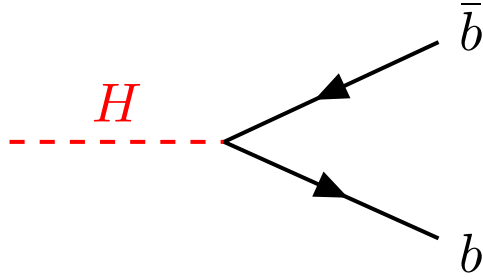
498 The coupling of the SM Higgs with the gauge bosons and fermions has been shown to
 499 give these particles their mass, however it also means that the Higgs can decay into all
 500 of these particles. In order of most to least likely final states of a Higgs decay we have

501 the decay to; a pair of b -quarks ($b\bar{b}$), a pair of weak vector bosons where one is off-shell
502 (VV^*), two gluons (gg), a duo of tau leptons ($\tau^+\tau^-$), or a pair of photons ($\gamma\gamma$). Similar
503 to the ggF production mechanism discussed in Section 3.1 the decays to massless gauge
504 bosons (photons and gluons) are facilitated through loops of massive particles. The
505 exact feynman diagrams depicting the above process' are shown in Figure 3.4 while
506 information about their branching ratios is detailed in Table 3.2.

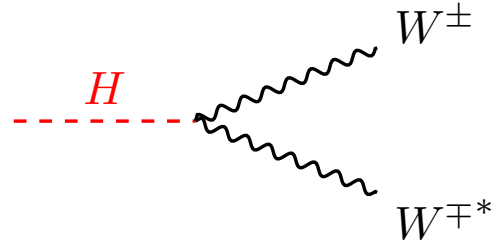
Table 3.2: The branching ratios and the relative uncertainty for a Standard Model Higgs boson with $m_H = 125$ GeV [1].

Decay Channel	Branching Ratio	Relative Uncertainty
$H \rightarrow b\bar{b}$	5.84×10^{-1}	+3.2% -3.3%
$H \rightarrow W^+W^-$	2.14×10^{-1}	+4.3% -4.2%
$H \rightarrow \tau^+\tau^-$	6.27×10^{-2}	+5.7% -5.7%
$H \rightarrow ZZ$	2.62×10^{-2}	+4.3% -4.1%
$H \rightarrow \gamma\gamma$	2.27×10^{-3}	+5.0% -4.9%
$H \rightarrow Z\gamma$	1.53×10^{-3}	+9.0% -8.9%
$H \rightarrow \mu^+\mu^-$	2.18×10^{-4}	+6.0% -5.9%

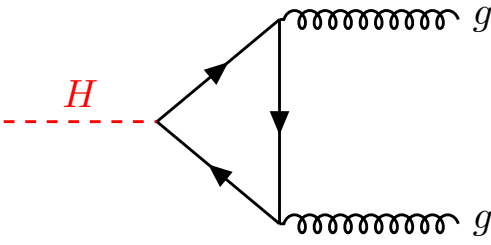
507 In Table 3.2 the order is determined by two distinct effects; the proportionality of the
508 Higgs couplings to the mass of the decay product, and whether or not the rest mass of
509 the higgs is sufficient to produce the two final state objects. In Figure 3.5 you can see
510 that as the mass of the higgs boson gets closer to $2m_W$ the cross section for $H \rightarrow WW$
511 grows.



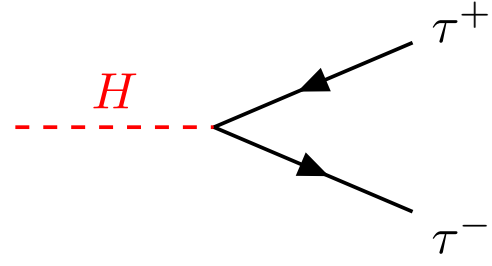
(a) $H \rightarrow b\bar{b}$



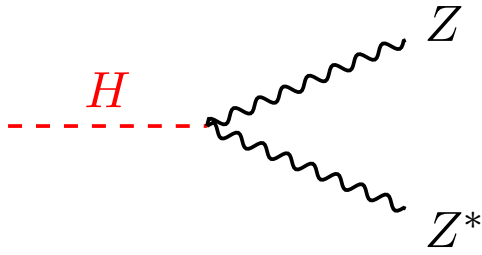
(b) $H \rightarrow W^{\pm}W^{\mp*}$



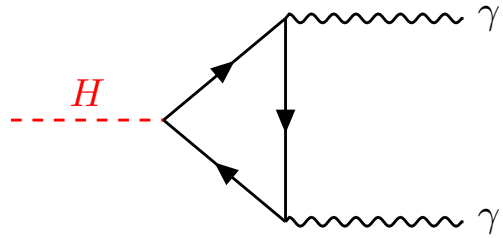
(c) $H \rightarrow gg$



(d) $H \rightarrow \tau^+\tau^-$



(e) $H \rightarrow ZZ^*$



(f) $H \rightarrow \gamma\gamma$

Figure 3.4: Feynman diagrams representing the leading Higgs decay channels.

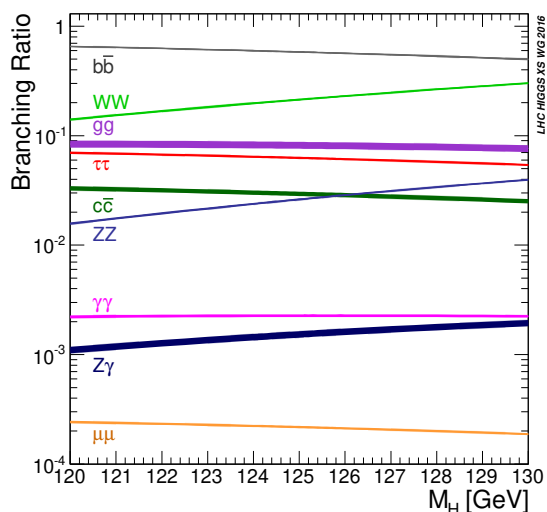


Figure 3.5: Branching ratios for the decay of the SM Higgs boson near $m_H = 125\text{GeV}$ including theoretical uncertainty bands [1]

3.4 Evidence for the SM Higgs

Using the above information about predicted final states the CMS and ATLAS experiment collaborations analyzed 5 fb^{-1} of LHC Run 1 data [3] to make measurements of the SM Higgs production cross-sections and branching ratios. The combined results of these studies can be seen in Figure 3.6 Figure 3.7 and Figure 3.8. Given the uncertainties on the measurements these results show good agreement between the predictions of the Standard Model and experiment with all best fit values falling within 2σ of the SM theoretical prediction.

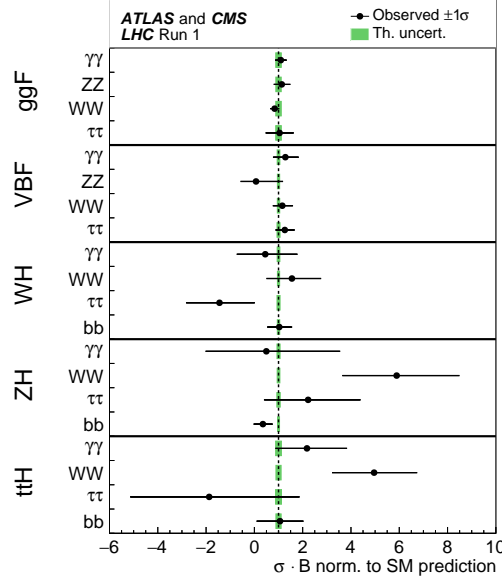


Figure 3.6: Best fit values of $\sigma_i \cdot B^f$ for each specific channel $i \rightarrow H \rightarrow f$, as obtained from the generic parameterisation with 23 parameters for the combination of the ATLAS and CMS measurements. The error bars indicate the 1σ intervals. The fit results are normalised to the SM predictions for the various parameters and the shaded bands indicate the theoretical uncertainties in these predictions. Only 20 parameters are shown because some are either not measured with a meaningful precision, in the case of the $H \rightarrow ZZ$ decay channel for the WH , ZH , and $t\bar{t}H$ production processes, or not measured at all and therefore fixed to their corresponding SM predictions, in the case of the $H \rightarrow b\bar{b}$ decay mode for the ggF and VBF production processes [3].

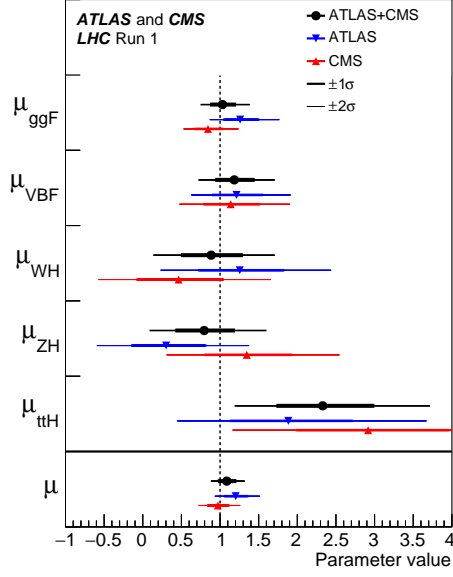


Figure 3.7: Best fit results for the production signal strengths for the combination of ATLAS and CMS data. Also shown are the results from each experiment. The error bars indicate the 1σ (thick lines) and 2σ (thin lines) intervals. The measurements of the global signal strength μ are also shown [3].

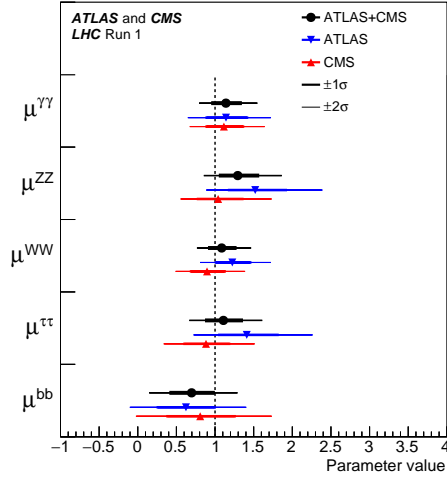


Figure 3.8: Best fit results for the decay signal strengths for the combination of ATLAS and CMS data. Also shown are the results from each experiment. The error bars indicate the 1σ (thick lines) and 2σ (thin lines) intervals [3].

3.5 Boosted Higgs

The strong agreement between the theoretical predictions of the SM Higgs boson and experiment shown in Section 3.4 represents the fulfillment of a generation of incredible technological and theoretical achievement. The next step is to push the search for deviations from the model that might hint at the physics of mysteries like the matter / anti-matter asymmetry of the universe, dark matter, the particle nature of gravity and dark energy.

Effective field theory arguments for extensions of the SM suggest that precise measurements of the shape of the momentum distribution for highly boosted (high momentum)

529 Higgs offer the opportunity to see the effects of natural new physics. In particular,
 530 at high enough energies – $p_{T,H} \geq 500$ GeV – the ggF production mode of the Higgs
 531 becomes sensitive to the heavy heavy fermion loop [4]. New resonances that run in
 532 the loop would contribute to the coupling strength of the effective gluon-gluon-Higgs
 533 interaction and would give an anomalous result compared to the SM. In references [4, 5,
 534 6] the effect on the production cross section for boosted Higgs through ggF can exceed
 535 50% for $p_{T,H} \geq 500$ GeV.

536 Searches for boosted Higgs are also made easier as the LHC produces a large number of
 537 soft (low momentum) QCD interactions. Thus a boosted signal is easier to differentiate
 538 from the common QCD interactions which fall off exponentially as a function of mo-
 539 mentum. However, to achieve this boost, the Higgs must recoil off of a high energy jet
 540 or photon [7] produced through initial state radiation (ISR) as seen in Figure 3.9 with
 541 $H \rightarrow b\bar{b}$. In this thesis only strongly produced ISR is considered in order to simplify
 542 the analysis.

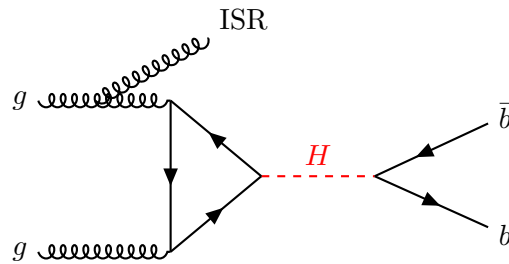


Figure 3.9: Feynman diagram for boosted Higgs decaying to $b\bar{b}$

543 As a result of this boost, the decay products of the Higgs and the hadronization products

544 of the ISR become highly collimated as shown in Figure 3.10. The two pronged structure
 545 of the jet that results from the $H \rightarrow b\bar{b}$ decay provides a unique signature that can be
 546 used to differentiate the Higgs signal from other QCD process.

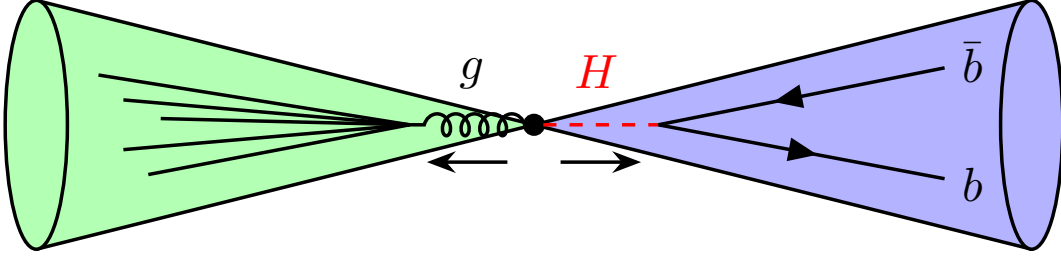


Figure 3.10: Cartoon showing collimated Higgs and ISR as a result of the large boost due to their mutual recoil.

547 In pursuit of the rich physics potential discussed above an analysis of Boosted Higgs
 548 signatures was undertaken and is discussed further in Part III.

549

Part II

550

Experimental Apparatus and

551

Associated Facilities

552 Chapter 4

553 The Large Hadron Collider

554 Located 100 meters under the Swiss / French border lies the 26.7 kilometer circumference
555 Large Hadron Collider (LHC) [8]. The culmination of a huge international collaboration,
556 this apparatus is used to produce proton and heavy ion collisions for observation by the
557 four major experiments at the LHC: ATLAS, CMS, LHCb, and ALICE. The system was
558 designed for a maximum center-of-mass energy of $\sqrt{s} = 14$ TeV and a peak instantaneous
559 luminosity of $L = 10^{34} \text{cm}^{-2} \text{s}^{-1}$.

560 The first LHC workshop was held in 1984 in Lausanne at the European Organization
561 for Nuclear Research (CERN) [9]. The nearly 30 year old case for a machine that
562 would push towards the discovery of the elusive Higgs Boson was presented using the
563 existing CERN accelerator facilities and the Large Electron Positron (LEP) collider
564 tunnel. The proposal became reality on September 10, 2008 when the first proton beams
565 were circulated, only to have calamity strike 9 days later in the form of a catastrophic

566 electrical fault. The repairs and improvements lasted until November 2009 when the
567 LHC restarted. Since then, this modern marvel has worked wonderfully and, as hoped,
568 lead to the discovery of the Higgs Boson by the ATLAS and CMS collaborations July
569 4, 2013.

570 The following chapter provides a brief introduction to the worlds most powerful accel-
571 erator starting with the little red bottle of hydrogen in building XXX, and ending with
572 the interaction point where protons collide at the highest energies ever produced.

573 4.1 Particle Injection Chain

574 We begin with the most common element in the Universe, hydrogen, as our source of
575 protons. A bottle of hydrogen gas provides 100 microsecond pulses of raw H_2 which
576 is then injected into a Duoplasmatron. There, a strong electric field and free electrons
577 from a cathode ionize the molecule into bare H^+ aka a proton! These protons are then
578 accelerated by a 90kV electric field, leaving the Duoplasmatron at 1.4% the speed of light
579 ($\sim 4000\text{km/s}$) or, in Particle Physics units, about 83KeV. The bare protons are then fed
580 into the accelerating Radio Frequency (RF) cavities of Linear Accelerator 2 (LINAC2).
581 Inside, conductors charged by a powerful oscillating electromagnetic field accelerate
582 the protons to an energy of 50MeV. Along the way, small quadrupole magnets shape
583 the proton bunch ensuring they remain in a tight beam. This pattern of acceleration
584 with RF cavities and shaping/tuning with magnets is then repeated with CERN's first

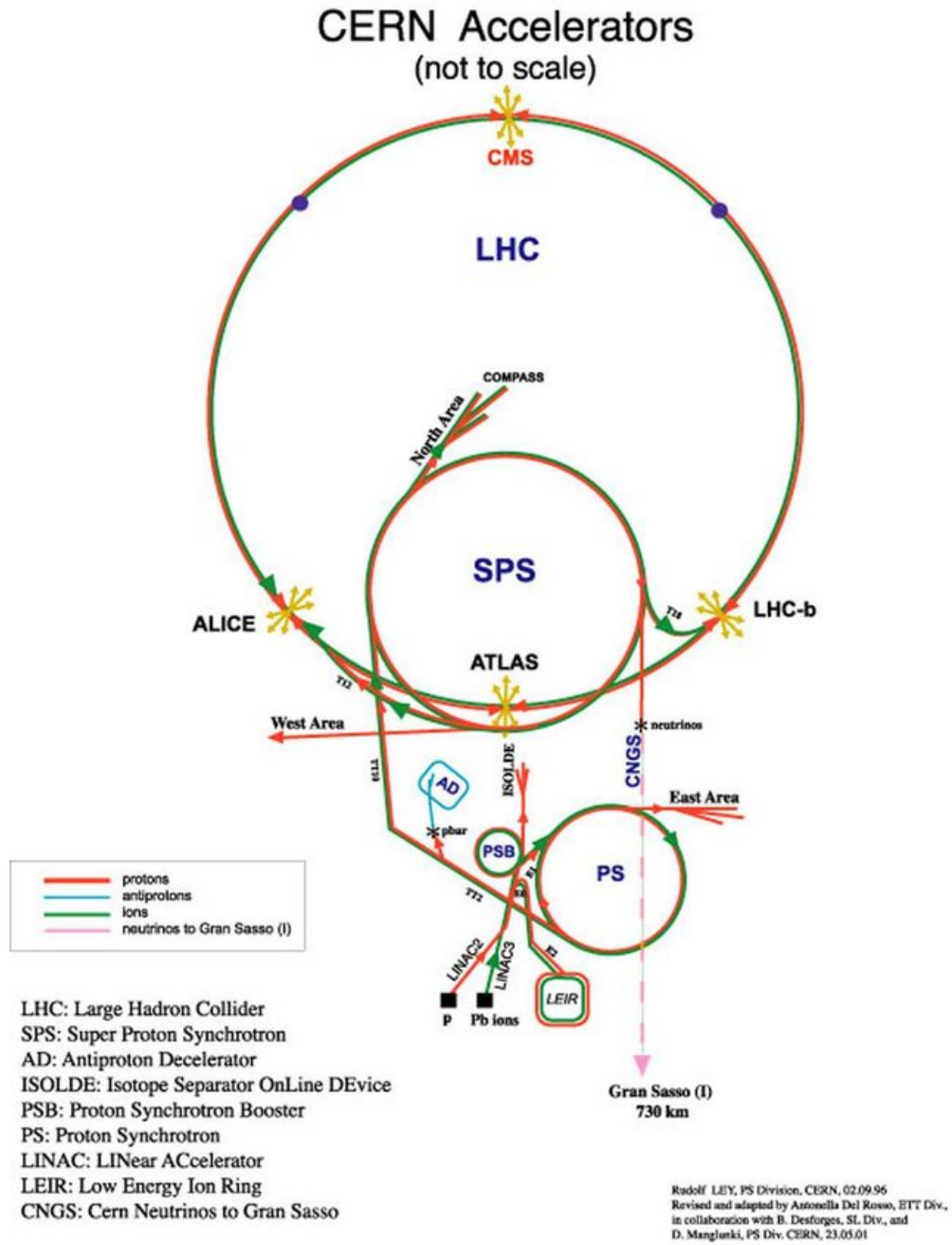


Figure 4.1: CERN accelerator complex

585 synchrotron, the Proton Synchrotron (PS) rendering a 1.4 GeV proton beam. The
586 final step before the LHC comes with the Super Proton Synchrotron where the same
587 technologies are implemented to produce 450 GeV protons, ready for injection into the
588 LHC. A diagrammatic representation of this chain can be seen in Figure 4.1.

589 In order to produce proton-proton collisions, the LHC uses two beams circulating in
590 opposite directions. The beams are not continuous, but instead consist of bunches of
591 $\mathcal{O}(10^{11})$ protons with a spacing of 25ns. Given the LHC circumference this allows for
592 3564 bunches, however only 2808 are filled per beam due to safety requirements and
593 injection limitations. Each beam takes 4 minutes and 20 seconds to fill and then an
594 additional 20 minutes to for the protons to reach their maximum energy of 7 TeV, or
595 99.99999991% the speed of light! Under normal operating conditions these beams can
596 be used for many hours.

597 **4.2 LHC Layout and Design**

598 While often depicted as a perfect circle the LHC is in reality an octagon with rounded
599 edges, called arcs, as can be seen in Figure 4.2. Here you can see the counter circulating
600 beams of protons depicted in red and blue. These beams are focused and collided at
601 the 4 dedicated interaction points at rates of up to 40 MHz. Two of these points are
602 occupied by the ATLAS and CMS experiments, both of which are high luminosity,
603 multi-purpose experiments.

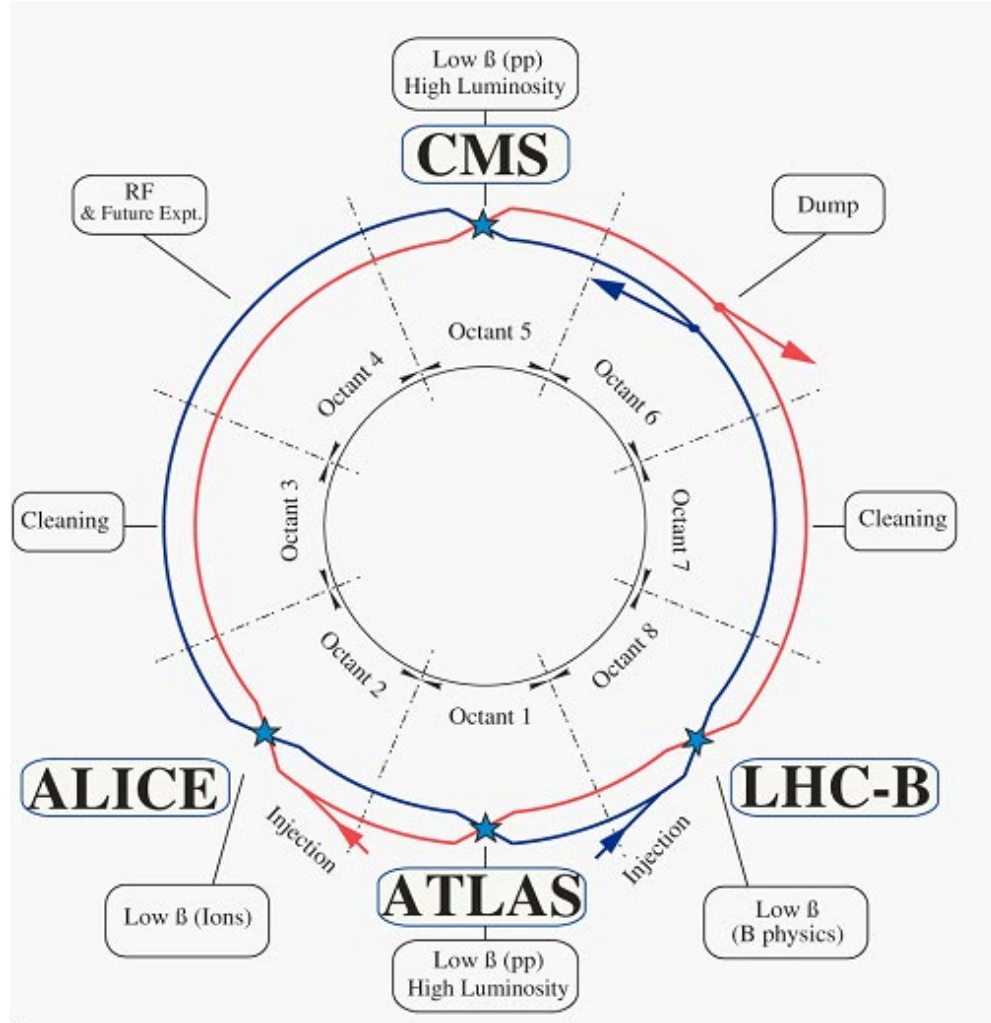


Figure 4.2: Labeled diagram of all the experiments at the LHC indicating the counter circulating beams and points of interest along the circumference of the accelerator.

604 The exact design of the LHC tunnel is due to the experimental constraints of the original
 605 machine for which it was built, the Large Electron Positron (LEP) Collider. For the
 606 $\sim 2,000$ times lighter electron the maximum energy was limited by the synchrotron
 607 radiation, proportional to $\frac{1}{m^4}$, requiring long straight sections of accelerating RF cavities
 608 to recuperate the lost energy. Given that this effect is $\mathcal{O}(10^{13})$ times smaller for the
 609 proton the LHC is instead limited by our ability to design and construct magnets strong
 610 enough to bend the beam given the already determined curvature of the 8 arcs.

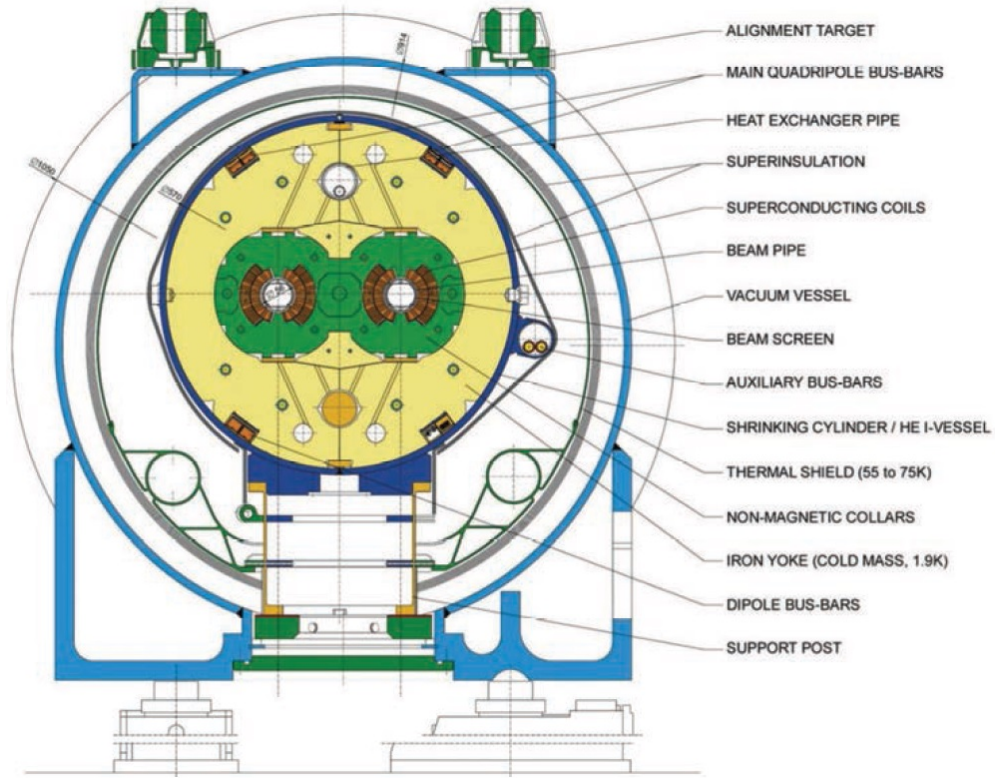


Figure 4.3: Depiction of a LHC dipole magnet 2-in-1 design labeling the major components

611 The oppositely circulating beams must each have their own ring and magnetic field
612 which lead to the creation of a twin-bore (i.e. "two-in-one") magnet design, a cross
613 section of which can be seen in Figure 4.3. These magnets are constructed using NbTi
614 superconductors which are cooled to 2K using superfluid helium. These magnets are
615 designed to provide the needed 8.33 T magnetic field required to bend the proton tra-
616 jectories at the designed beam energy of 7 TeV. In total 1231 of these 15 m bending
617 dipole magnets are used, in association with 392 5-7m quadrupole magnets which are
618 responsible for keeping the proton bunches in a tight beam by squeezing them both
619 horizontally or vertically.

620 4.3 Performance

621 Since the begining of its stable running in 2010 the LHC has performed well, exceeding
622 expectations. While the experiment itself is incredibly complex, the performance of the
623 machine, for the purposes of our analysis, can be reduced to two numbers; the familiar
624 center of mass energy of the beams and a less common quantity known as the integrated
625 luminosity.

626 For particle physics the integrated luminosity is proportional to the total number of
627 collisions recorded during a specified time period, while the instantaneous luminosity is
628 proportional to the bunch crossing rate along with the cross section of a proton-proton
629 interaction and represents the potential number of collisions per second. Knowing this

630 we can see that the integrated luminosity, L_{int} is simply the integral of the instantaneous
631 luminosity $L_{inst.}$ for a choosen data period as seen in Equation (4.1).

$$L_{int} = \int L_{inst.} dt \quad (4.1)$$

632 For a standard Gaussian beam, $L_{inst.}$ can be written as

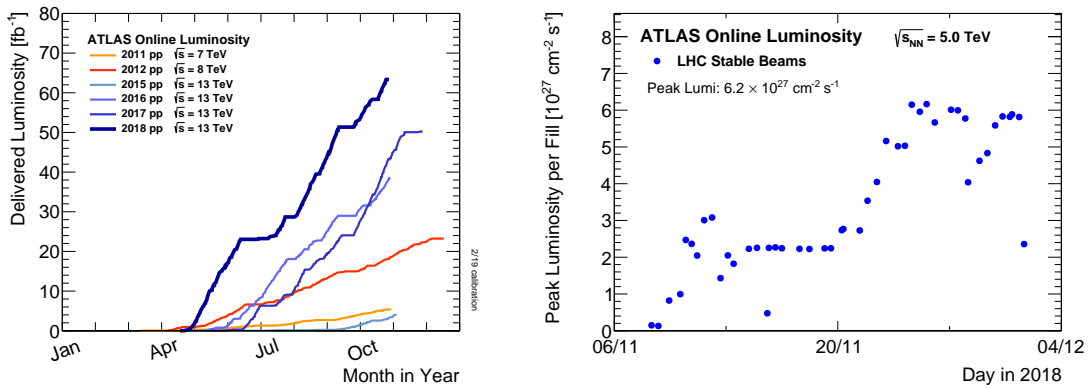
$$L_{inst.} = \frac{N_b^2 n_b f_{rev} \gamma_r}{4\pi \epsilon_n \beta^*} F \quad (4.2)$$

633 where N_b is the number of particles per bunch, n_b the number of bunches per beam,
634 f_{rev} the revolution frequency, γ_r the relativistic gamma factor, ϵ_n the normalized trans-
635 verse beam emittance, β^* the beta function at the collision point, and F the geometric
636 luminosity reduction factor due to the crossing angle at the interaction point given by

$$F = \left(1 + \left(\frac{\theta_c \sigma_z}{2\sigma^*} \right)^2 \right)^{-1/2} \quad (4.3)$$

637 where θ_c is the full crossing angle at the interaction point, σ_z is the RMS bunch length,
638 and σ^* is the transverse RMS beam size at the interaction point.

639 For the ATLAS experiment the integrated luminosity for each year can be seen in
640 Figure 4.4a as well as an example of the instantaneous luminosity for the choosen year
641 in Figure 4.4b.



(a) Integrated Luminosity 2011 - 2018 (b) 2018 Peak Instantaneous Luminosity

Figure 4.4: Luminosity is monitored as both a running total known as the Integrated Luminosity as depicted in (a) and as an instantaneous quantity as shown in (b).

642 4.4 Pile-up at the LHC

643 Given the large number of protons per bunch and the cross-section of a proton-proton
 644 interaction, the probability to observe multiple interactions per bunch crossing is quite
 645 high. These multiple-interaction are known as pile-up, μ or the time-averaged represen-
 646 tation $\langle\mu\rangle$, and comes in two different forms:

- 647 1. **In-time pile-up:** These are the other proton-proton collisions that occur during
 648 the same bunch crossing as the primary interaction that caused the Data Aquisi-
 649 tion (DAQ) system to trigger. These are the standard extra interactions we expect
 650 to observe as stated above.
- 651 2. **Out-of-time pile-up:** These are interactions that occur either before or after a

652 bunch crossing that causes the DAQ to trigger. This effect is generally due to the
 653 long integration times of some detector electronics.

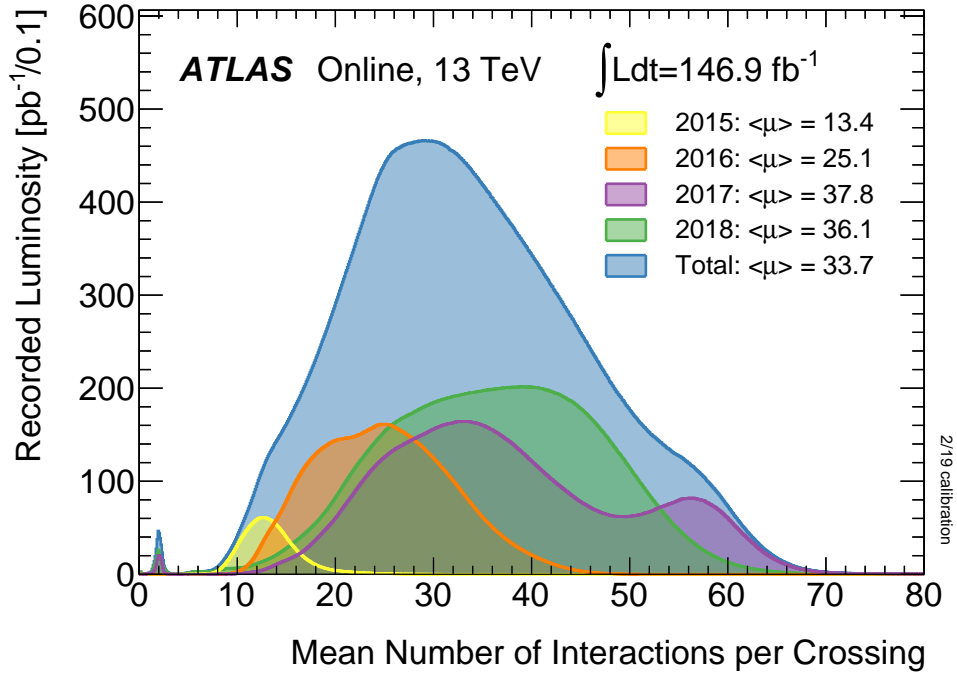


Figure 4.5: Pileup for data taking periods 2015 - 2018

654 The pile-up profile for past years can be seen in Figure 4.5. The width of this distributino
 655 is due a combination of Poissonian statistics, the decrease in number of protons per bunch
 656 over the lifetime of a single run, and optimization tweaks to the beam's profile during
 657 the LHC's operation. Understanding and eliminating the noise from these pile-up events
 658 is crucial to reconstructing physics variables that describe the primary interaction we
 659 aim to observe.

Chapter 5

The ATLAS Detector

Given the immense energies available at the LHC, and the veritable zoo of particles we are trying to detect, we require a general-purpose experiment in order to fully exploit the full range of physics opportunities provided. Two international collaborations rose to this challenge, the CMS (Compact Muon Solenoid) and ATLAS (A Toroidal LHC Apparatus) experiments. While both have similar physics goals and each of them strengths and weaknesses, this dissertation will focus on the ATLAS experiment and the intricacies of its three sub-detectors and two massive magnet systems depicted in Figure 5.1.

Originally proposed in 1994, the ATLAS detector was completed in 2008. On July 4th, 2012 in a joint announcement the ATLAS and CMS experiments presented the discovery of the long predicted Higgs Boson. The ATLAS collaboration now boasts over 3000 physicists from 175 institutions spread across 38 countries and continues to

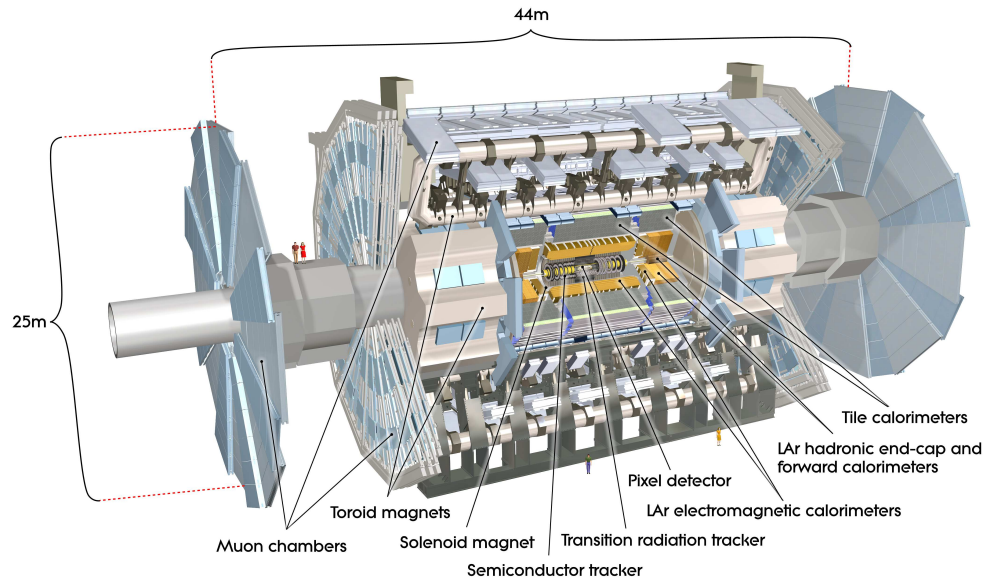


Figure 5.1: [10] Here we see a cut-away side view of the ATLAS detector with the major components labeled. Note that within each of these labeled components there may exist multiple different detector technologies. For scale two people in red are shown standing between the disk muon chambers on the left side of the figure.

674 probe the limits of the Standard Model in pursuit of answers to some of humanity's
675 deepest questions.

676 Located approximately 100 meters underground in a vast excavated chamber, the AT-
677 LAS detector rests its 7000 metric tons on a bed of concrete-reinforced steel. Out of it
678 flows the signals from 100 million electronic channels through a zip-tied mass of 3000+
679 kilometers of cabling. At its very center is one of the four interaction points of the
680 LHC, specifically Point 1, where the two counter circulating proton beams are shaped
681 and then brought together by a series of magnets. The energetic particles resulting from
682 this collision then fly out in all directions into the bulk of the ATLAS detector.

683 The first sub-system they meet is the Inner Detector (ID) and its many layers of strip and
684 pixel silicon detectors along with a transition radiation gaseous wire detector, all bathed
685 in the 2T magnetic field from the surrounding superconducting solenoidal magnet.
686 This system exploits the ionization of charged particles to track their curved trajectory
687 through the magnetic field. This curvature gives us charge information, a momentum
688 measurement, and precisely-located 3D vertices crucial to the identification of the sec-
689 ondary vertices of a B-hadron decay.

690 Outside of the solenoid the particles encounter the Electromagnetic and then the Hadronic
691 sampling calorimeters. Here, layers of scintillator and high radiation length materials
692 are implemented to measure the energy of electrons, photons, and hadrons. As the goal
693 is to completely absorb the energy of all outgoing particles the calorimeter has a nearly
694 4π solid angle coverage.

695 Finally we have the muon system surrounding the calorimeter and equipped with its
696 own toroidal magnet system. Here the charged muon bends in the magnetic field while
697 leaving a trail of ionization in the Muon Spectrometer before exiting the detector com-
698 pletely. Neutrinos are the only other Standard Model particle that leave the detector,
699 however they do so without detection. A depiction of the various particle interactions
700 with the different detector sub-systems can be seen in Figure 5.2

701 In the following sections I will explain our chosen coordinate system and give a more
702 detailed review of these three detector sub-systems.

703 5.1 ATLAS Coordinate System

704 Using the nominal interaction point as the origin, ATLAS uses a right-handed coordi-
705 nate system where the positive x -axis points towards the center of the LHC ring,
706 the positive y -axis points upwards, and the positive z -axis is defined by the counter
707 clockwise circulating beam direction as viewed from above shown in Figure 5.3 [10].

708 Using these coordinates we can define the physical momentum of the objects measured
709 as $\vec{p} = (p_T, p_z)$ with p_T being the momentum of the object in the transverse plane and
710 p_z the momentum along the beam axis. Given the cylindrical symmetry of ATLAS it
711 is desirable to define the polar angle θ from the beam axis with the r - ϕ plane being
712 perpendicular to that axis. Since the particles we observe are relativistically boosted in
713 the z -axis it is desirable to use the Lorentz invariant quantity pseudorapidity (η) defined

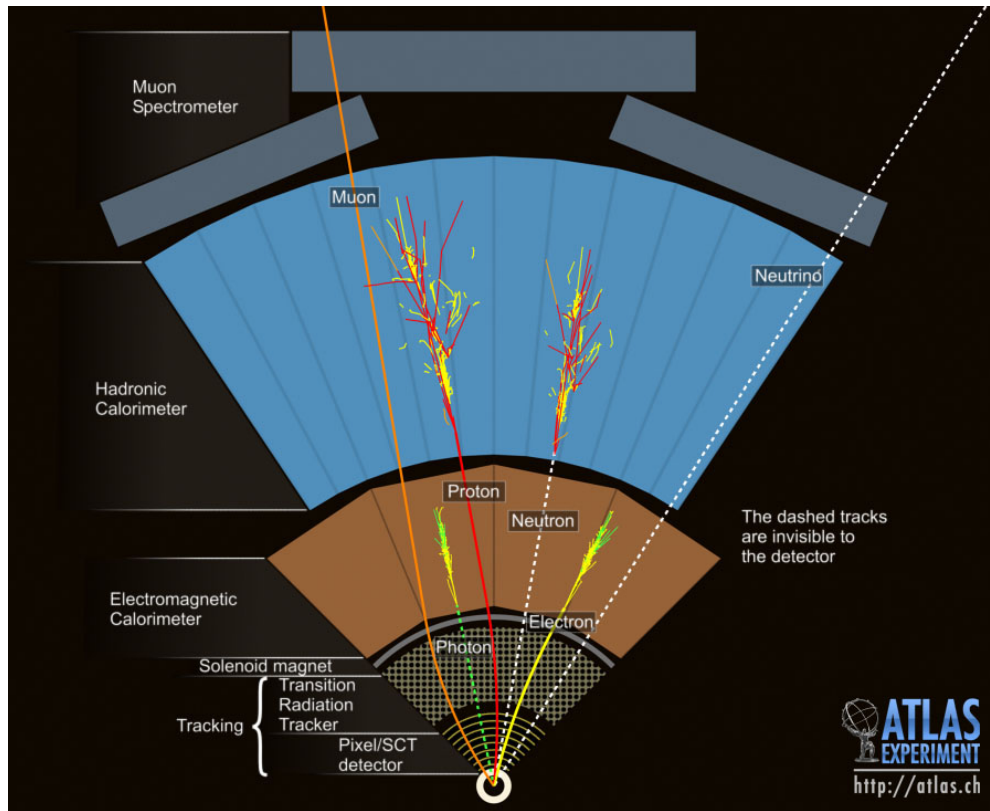


Figure 5.2: This slice of the ATLAS detector depicts how different particles interact with each component of the detector it crosses. A dashed line indicates no interaction while a solid line indicates interaction. Electrons (yellow/green) and charged hadrons (red) interact with the tracker and curve in the solenoid's magnetic field. Electrons and photons (yellow/green) are absorbed by the Electromagnetic calorimeter. All hadrons (red/yellow) are absorbed by the Hadronic calorimeter. The muons (orange) curve in both the solenoid and toroid magnetic fields before exiting the detector. Finally, the neutrinos (white) pass through the entire detector without interacting.

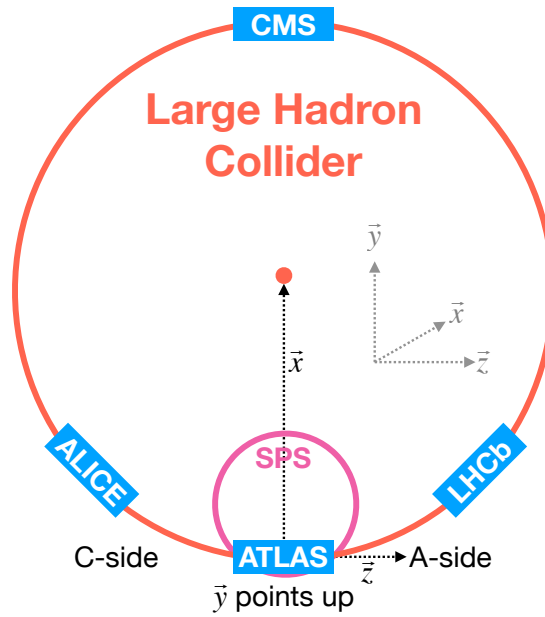


Figure 5.3: [11] A cartoon view of the the LHC from above showing the SPS, LHC and the four main experiments of the LHC: ATLAS, CMS, LHCb, and ALICE. The standard cartesian coordinate system is shown with its origin at the ATLAS interaction point, the positive x -axis towards the center of the LHC, the positive y -axis pointing upwards, and the positive z -axis pointing along the beamline towards the "A-side"

714 in terms of the polar angle by

$$\eta = -\ln \tan \left(\frac{\theta}{2} \right). \quad (5.1)$$

715 where $\eta = 0$ is in the x - y plane and larger values of $|\eta|$ being closer to the beam axis as

716 can be seen in Figure 5.4.

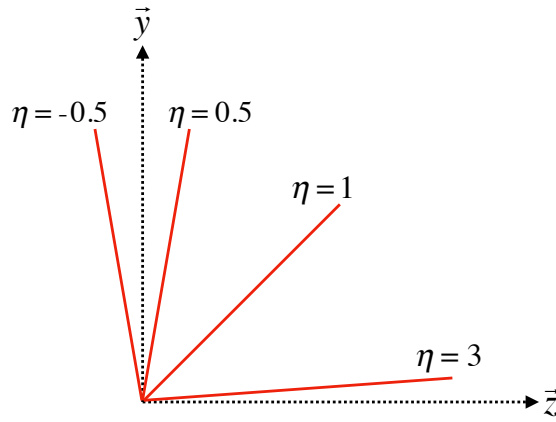


Figure 5.4: Modified from [11] this cartoon represents a selection of pseudorapidity (η) values overlaid with some cartesian coordinates (dashed black lines). The red lines are drawn for $\eta = \pm 0.5, 1.0, 3.0$

717 In this analysis the angular separation between objects in the detector is calculated and

718 represented using the geometric quantity

$$\Delta R = \sqrt{(\Delta\eta)^2 + (\Delta\phi)^2} \quad (5.2)$$

719 5.2 Tracking with the Inner Detector

720 With its closest component, the Insertable B-Layer (IBL) [12], only 3.3 cm from the
 721 interaction point. The Inner Detector (ID), shown in Figure 5.5 [13, 14], faces the in-
 722 credible challenge of providing precise momentum resolution and identification of both
 723 primary and secondary vertex measurements of charged particle tracks all while receiv-
 724 ing the highest fluence.

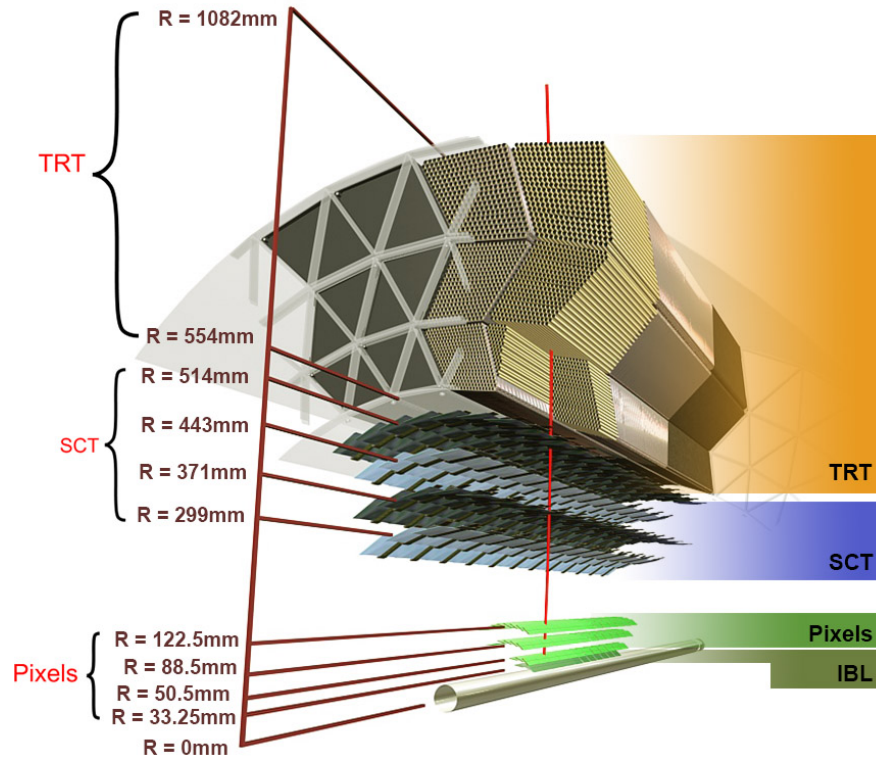


Figure 5.5: [12] Diagram of inner detector

725 It is designed to be very compact to reduce the probability of a particle decaying inside
 726 and to give precision measurements of the particles curvature in the 2T solenoidal

727 magnetic field. This leads to excellent momentum resolution above the nominal p_T
728 threshold of 0.5 GeV and within the pseudorapidity range of $|\eta| < 2.5$ as shown in
729 Figure 5.6.

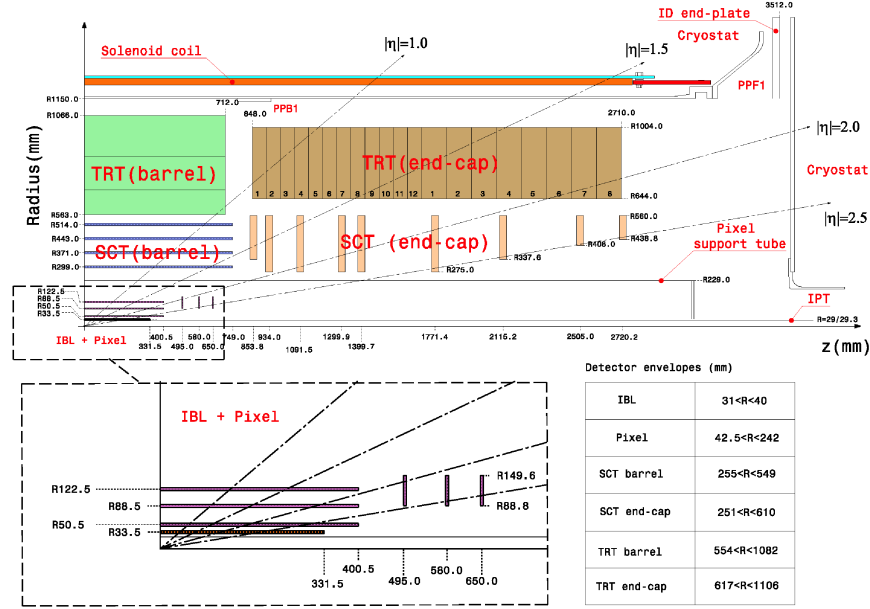


Figure 5.6: [15] Schematic of the Inner Detector including η lines. Each component shown is cylindrically symmetric leading to a multi-layered detector.

730 The ID is composed of three different detector technologies for particle trajector recon-
731 struction: Pixel Detector, Semiconductor Tracker (SCT) and the Transition Radiation
732 Tracker (TRT). These will be discussed in the following sections.

733 5.2.1 Pixel Detector

734 The ATLAS Pixel Detector [10], the innermost subdetector of the ID, is designed to
735 give the best resolution possible as close as possible to the interaction point. This is
736 accomplished using the 4 barrel layers and 3 disks per endcap as indicated in Figure 5.6.
737 The innermost barrel layer, the IBL, has pixel dimensions of $50\mu\text{m}(\hat{\phi}) \times 250\mu\text{m}(\hat{z}) \times$
738 $200\mu\text{m}(\hat{r})$. For the other layers the dimensions are $50\mu\text{m}(\hat{\phi}) \times 400\mu\text{m}(\hat{z})$ for about 90%
739 of the pixels and $50\mu\text{m}(\hat{\phi}) \times 600\mu\text{m}(\hat{z})$ for the others, all with a thickness of $250\mu\text{m}(\hat{r})$.
740 This gives a total active area of 1.88m^2 collected through 92.4 million readout channels,
741 more than half of the total number of channels for ATLAS. This detailed charged particle
742 information very close to the interaction point is crucial not only for pattern recognition
743 and track reconstruction, but also for the reconstruction of the primary and secondary
744 vertices intrinsic to the decay of b -hadrons, a critical element of the analysis presented
745 in this thesis.

746 5.2.2 Semiconductor Tracker

747 Encompassing the Pixel Detector, the Semiconductor Tracker (SCT) [10] is composed of
748 double-sided silicon microstrip modules. Each side of the 4088 modules is constructed
749 out of two silicon strip sensors that are daisy-chained together. The result is 768
750 composite strips each 12.6cm with an inter-strip pitch of $80\mu\text{m}$. In the barrel the strips
751 are aligned with the \hat{z} direction, while in the end-caps they are aligned with the \hat{r}
752 direction. In both cases the separation of the strips is constant in $\hat{\phi}$. The two sides are

rotated with respect to each other by $40\mu\text{m}$ to allow for position measurement along the length of the strip. These modules are then used to tile the 4 barrel layers and 9 disks per endcap (18 disks in total) as seen in Figure 5.6. This design is chosen to ensure that each charged track interacts with 8 strip layers (equivalent to four space points). This information is used to further measure the momentum and impact parameter, as well as vertex identification of charged particles.

5.2.3 Transition Radiation Tracker

The Transition Radiation Tracker [10], the outermost subdetector of the ID, provides tracking through the detection of transition radiation from ultra-relativistic charged particles for $\eta < 2.0$ using 350,000 drift tube channels also known as straws. The 4mm diameter straws are filled with a 70% Xe, 27% CO₂, and 3% O₂ gas mixture and a $31\mu\text{m}$ diameter gold-plated tungsten wire anode at the center for the collection of the ionization signal. In the barrel 73 azimuthally symmetric layers of 144cm straws are oriented parallel to the beam pipe with an electrical division in the center of each allowing the two sides to be read out separately. For each endcap the straws are radially oriented in 160 symmetric planes each containing 37cm long drift tubes shown in Figure 5.6. In both the barrel and the endcaps polypropylene fibers (barrel) or foils (encaps) function as the transition radiation material which causes the relativistic charged particles to radiate and thus ionize the gas in the straw. The amount of transition radiation produced is proportional to the Lorentz factor meaning that lighter particles (e.g. electrons) will

773 produce more radiation. Thus, by defining a high and low threshold, we can identify
 774 tracks belonging to electrons by requiring they register more high-threshold hits. There
 775 are typically 36 TRT hits per charged particle track.

776 5.3 Calorimetry

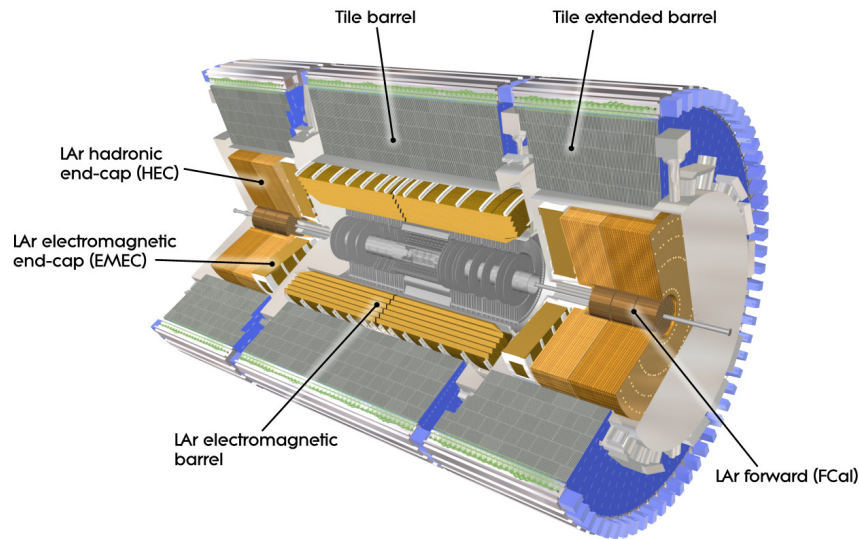


Figure 5.7: [10] A cutaway diagram of ATLAS sampling calorimeters

777 Once the proton-proton collision remnants have passed through the ID and its surround-
 778 ing solenoid they enter into the ATLAS calorimeters depicted in Figure 5.7. Sampling
 779 calorimeter technologies were chosen for their compact geometry and lower cost point.
 780 These are constructed by alternating layers of absorber, a dense material which reduces
 781 the incident particles energy, and active material which produces a detectable signal
 782 when a particle passes through. This means that the detected signal is only a fraction

of the total energy of the particle and thus requires a study of the calorimeter response
 for calibration purposes [16]. The first system, the Electromagnetic Calorimeter (EMC),
 is designed to measure the energy of electrons and photons which primarily lose their
 energy via bremsstrahlung and pair production electromagnetic interactions. Outside
 of the EMC is the Hadronic Calorimeter (HCal) which is designed to measure the en-
 ergy of jets of hadrons through their electromagnetic and strong interactions. These
 detectors cover the entire $|\eta| < 4.9$ range and provide complete containment of both
 Electromagnetic and Hadronic showers with higher granularity in the EMC for $|\eta| < 2.5$,
 the region matched to the ID, for precision measurements of electrons and photons. By
 instrumenting this huge space in $|\eta|$ we can search for events with asymmetric energy
 deposits which imply the existence of a particle we didn't detect represented by missing
 transverse energy E_T^{miss} .

5.3.1 Electromagnetic Calorimeter

The innermost calorimeter, the Liquid Argon (LAr) Electromagnetic Calorimeter (EMC)
 [10], uses Lead as the absorber and Liquid Argon as the active material in an "accor-
 dion geometry" as seen in Figure 5.8. This geometry was chosen for uniform coverage
 in $\hat{\phi}$ due to its lack of un-instrumented cracks in the radial direction. The barrel region
 covers $|\eta| < 1.475$ and an end cap on each side covers $1.375 < |\eta| < 3.2$ each housed
 in their own cryostat. The barrel is composed of two half barrels with a 4mm gap at
 $z = 0$ and both end caps are divided into an inner wheel covering $2.5 < |\eta| < 3.2$ and

803 an outer wheel covering $1.375 < |\eta| < 2.5$.

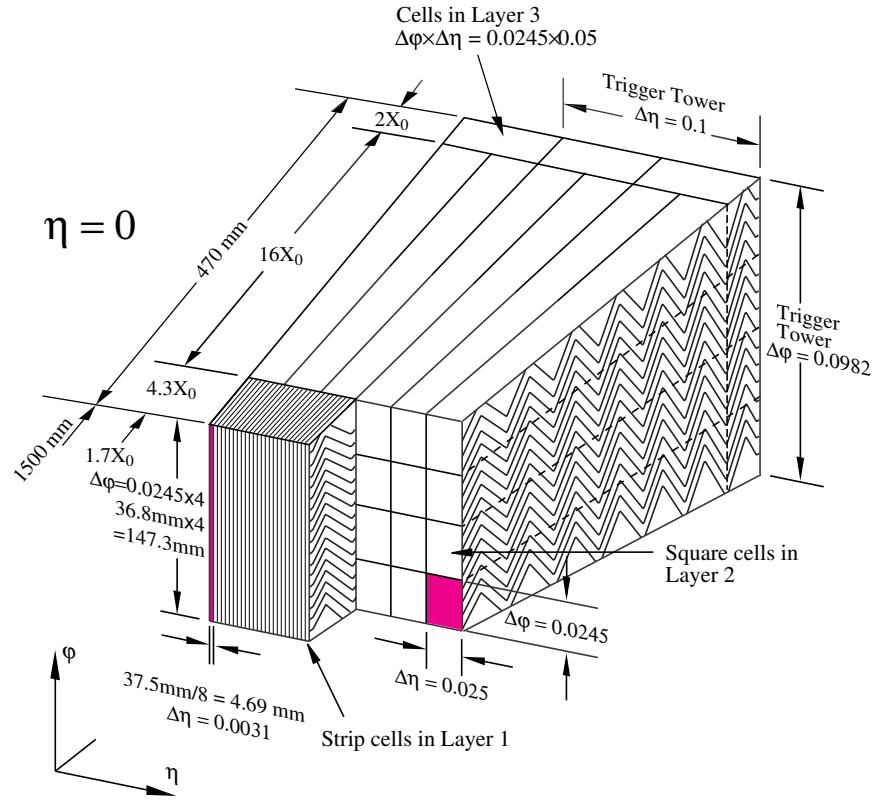


Figure 5.8: [10] Sketch of LAr EMC barrel module where the lead and liquid argon layers are visible in an accordion like geometry. Looking from the foreground to the back there are 3 different types of cells visible.

804 In the $|\eta| < 2.5$ region the EMC has 3 radial layers for precision physics measure-
 805 ments. Layer 1 consists of strip cells which are finely segmented with $\Delta\eta = 0.0031$
 806 and $\Delta\phi = 0.0245$ allowing for precision position resolution which gives discrimination
 807 power between a single γ deposit and the π^0 characteristic $\gamma\gamma$ deposit. Layer 2 , which
 808 collects the largest fraction of energy from electromagnetic shower, is segmented with

809 $\Delta\eta = .025$ and $\Delta\phi = 0.0245$. Layer 3 collects the tail of the electromagnetic shower
 810 using a coarser segmentation of $\Delta\eta = .05$ and $\Delta\phi = 0.0245$. Additionally, in the region
 811 $|\eta| < 1.8$ a thin pre-sampler, which contains no lead absorber, was placed in front of
 812 Layer 1 to allow for energy corrections due to losses upstream of the EMC. Combined
 813 the EMC is > 22 radiation lengths (X_0) in the barrel and $> 24 X_0$ in the end-caps,
 814 where a radiation length is the average distance an electron travels in a given material
 815 before losing $1/e$ of its original energy E_0 via bremsstrahlung radiation.

816 **5.3.2 Hadronic Calorimeter**

817 Directly outside the EMC envelope is the Hadronic Calorimeter (HCal) system [10]
 818 which consists of three sampling calorimeter technologies: the Tile calorimeter, the
 819 LAr hadronic end-cap calorimeter (HEC) and the LAr forward calorimeter (FCal).
 820 Combined, these three subsystems give measurements of hadronic jet energies in the
 821 $0 < |\eta| < 4.9$ range. The tile calorimeter uses steel as the absorber layer and scintillating
 822 tiles as the active material and covers the region $|\eta| < 1.7$ with a barrel section flanked
 823 by two barrel extensions each divided azimuthally into 64 modules. These scintillator
 824 tiles are read out on two sides by wavelength shifting fibers connected to photomulti-
 825 plier tubes as seen in Figure 5.9. At $\eta = 0$ the total tile calorimeter thickness is 9.7
 826 nuclear interaction lengths (λ), where λ is the average distance a hadron travels before
 827 interacting inelastically with a nucleus.

828 The HEC is composed of two independent wheels per end-cap located just past the

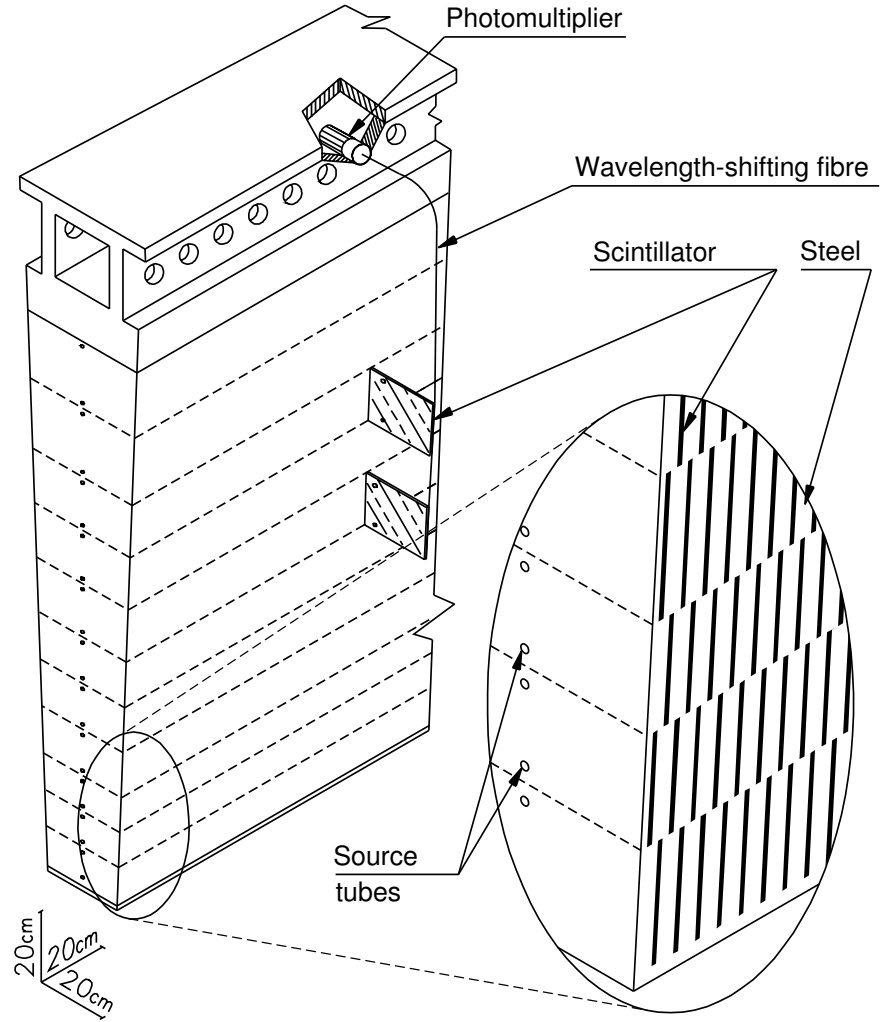


Figure 5.9: [10] Schematic of a tile calorimeter module including a depiction of the connection between the scintillator tile to the photomultiplier via a wavelength-shifting fibre.

829 EMC end-cap but sharing the same cryostat. This system uses copper as an absorber
 830 and liquid argon for the active material and covers the $1.5 < |\eta| < 3.2$ range using
 831 32 wdg-shaped modules per wheel. Finally, the FCal shares the same cryostat as the
 832 EMC and HEC end-caps and acts to extend the coverage of the combined calorimeter
 833 system to include the $3.1 < |\eta| < 4.9$ range. Each endcap contains 3 modules, the first
 834 an electromagnetic module (Copper/Liquid-Argon) which is followed by two hadronic
 835 modules which use (Tungsten/Liquid-Argon).

836 **5.4 Muon Spectrometer**

837 The ATLAS Muon Spectrometer (MS) [10], see Figure 5.10, accomplishes tracking of
 838 muons in the $|\eta| < 2.7$ region for momentum reconstruction while also triggering on
 839 charged particles in the $|\eta| < 2.4$ region. The magnetic field necessary for momentum
 840 reconstruction is provided by 3 air-core toroid systems, one barrel toroid covering $|\eta| <$
 841 1.4 and two endcap toroid systems which are inserted into the inner radius of the the
 842 barrel toroid to cover the $1.6 < |\eta| < 2.7$. The so called transition region $1.4 < |\eta| < 1.6$
 843 between these two magnet systems is covered by a combination of the barrel and endcap
 844 toroid magnets. Similar to the ID the resolution is inversely proportional to the particle's
 845 incident momentum. Any muon with p_T lower than 3GeV will never make it to the
 846 MS and thus will not be detected.

847 Precision tracking measurements for momentum reconstruction is accomplished using

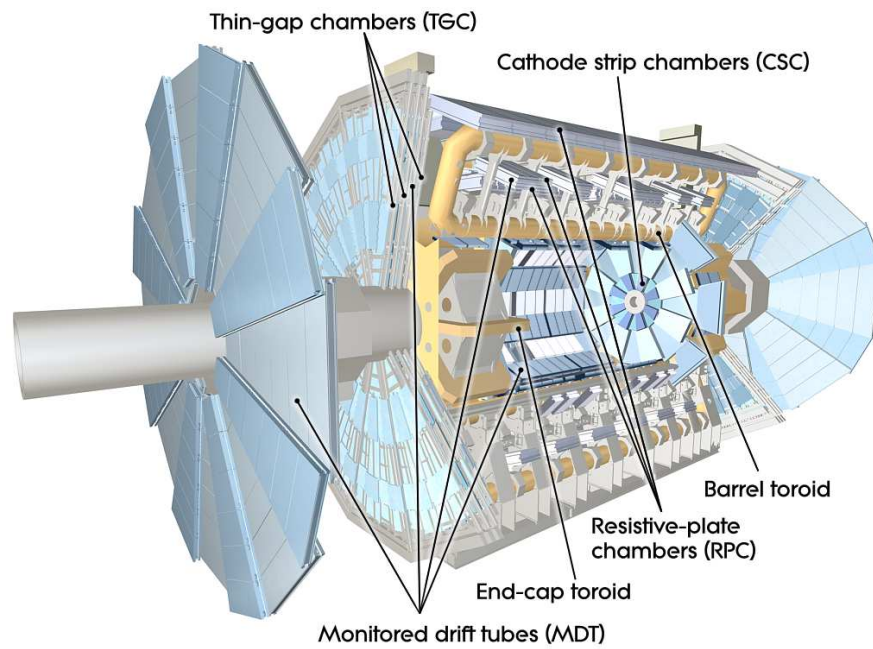


Figure 5.10: [10] A cut-away diagram of the ATLAS muon system and its many sub-detectors.

848 the Monitored Drift Tube chambers (MDTs) for $|\eta| < 2.0$ and using Cathode-Strip
849 Chambers (CSCs) for $2.0 < |\eta| < 2.7$. The MDT system consists of 1163 drift tube
850 chambers arranged in three to eight layers for varying η . The CSCs are designed to
851 withstand the higher rate and retain good time resolution using multiwire proportional
852 chambers with orthogonal segmented cathode planes.

853 The MS also gives nanosecond tracking information for triggering on muon tracks. This
854 is accomplished using Resistive Plate Chambers (RPC) in the barrel region $|\eta| < 1.05$
855 and Thin Gap Chambers (TGC) in the end-cap $1.05 < |\eta| < 2.4$ region. Both chamber
856 systems deliver a triggerable signal with a spread of 15–25 ns, thus providing the ability
857 to tag individual beam-crossings.

Part III

The HbbISR Analysis

Chapter 6

Data and Monte-Carlo Simulation

This analysis focuses on the data collected by the ATLAS detector from pp collisions produced by the LHC at the center-of-mass-energy of 13 TeV. In particular the analysis shown uses datasets collected in 2015, 2016, and 2017 and amounts to an integrated luminosity of 80.5 fb^{-1} after beam, detector and data-quality requirements are taken into account.

In order to compare our findings with theory, we use the predictions of the SM to produce Monte-Carlo (MC) simulated events to model the signal and background processes. These MC samples go through a full simulation of the ATLAS detector and are processed such that the MC and Data have the same format at analysis level. This allows us to analyze the MC and Data using the same framework such that we can make direct comparisons between theory and reality as our final product.

6.1 Data Used

As mentioned before the data used is checked to make sure it is of high quality, meaning that the beam, detector and data collection systems were all fully operational during the event in question. These data quality requirements are enforced by choosing only events from each respective years Good Runs List (GRL), an XML file produced by the ATLAS data quality monitoring team that lists all events that have met the data quality criteria. This analysis uses three such GRLs - one for each year of data taking (2015,2016,2017) - corresponding to annual integrated luminosities of 3.2 fb^{-1} , 33 fb^{-1} , and 44.3 fb^{-1} .

6.2 Signal Monte Carlo

In order to simulate Boosted Higgs events the three leading production mechanisms at the LHC were considered, shown in Figure 3.2: gluon-gluon fusion, vector boson fusion and Higgstralungh. These three production modes correspondingly represent 50%, 30% and 20% of the total Higgs signal before analysis cuts are applied.

The ggF plus an associated jet events were generated using the HJ+MINLO prescription [17] with the finite top mass assumption with the POWHEG-BOX 2 generator [Campbell:2012] and the NNPDF30 NNLO parton distribution function [18]. After the events are generated the

891 **6.3 Background Monte Carlo**

892 **Chapter 7**

893 **Physics Object Selection**

894 After the ATHENA Digitization step both data and monte carlo have the same format,
895 representing the three dimentional energy deposits. In order to analyze these deposits
896 they are cleaned, clustered and checked for overlap resulting in physics objects useful
897 for our specific analysis.

898 **7.1 Calorimeter Jets**

899 **7.2 Track Jets**

900 **7.3 Fat Jets**

901 **7.4 B-tagged Jets**

902 **7.5 Muons**

903 **7.6 Overlap Removal**

904 **Chapter 8**

905 **Event Selection**

906 Having created our physics objects we begin to make selections of what types of events
907 we want to consider given the goal of our analysis. In our boosted topology this means
908 considering things like momentum, jet collection efficiencies and background rejection.

909 **8.1 Selected Triggers**

910 **8.2 Pre-selection Studies**

911 **8.3 Signal Selection**

912 **8.4 Optimisation**

913 Chapter 9

914 Background Estimation

915 The dominant background was QCD. I worked on the $t\bar{t}$ control region. The V_{qq}
916 and single top backgrounds were estimated from monte carlo.

917 9.1 Multi-jet QCD estimation

918 9.2 $t\bar{t}$ control region

919 9.3 Single top estimation

920 9.4 Hadronic vector boson channel

921 **Chapter 10**

922 **Systematic Uncertainties**

923 **10.1 Theoretical Uncertainties**

924 **10.2 Experimental Uncertainties**

925 **Chapter 11**

926 **Statistical Fit**

927 The statistical fit in our analysis was accomplished using a framework developed for
928 Higgs searches.

929 **11.1 Profile Likelihood Function**

930 **11.2 Fit Configuration**

931 **11.3 Statistical Tests**

932 **Chapter 12**

933 **Results**

934 **12.1 Expectations**

935 **12.2 Statistical Analysis Results**

936 **12.3 Measurements and Limits**

937

Part IV

938

Conclusion

939 Chapter 13

940 Conclusion

941 I conclude that this section is the conclusion

Bibliography

- [1] Particle Data Group. “Review of Particle Physics, Chapter 11: Status of Higgs Boson Physics”. In: *Phys. Rev. D* 98 (3 2018), p. 030001. DOI: 10.1103/PhysRevD.98.030001. URL: <https://link.aps.org/doi/10.1103/PhysRevD.98.030001> (cit. on pp. 22, 24, 27, 29).
- [2] L. A. Harland-Lang et al. “Parton distributions in the LHC era: MMHT 2014 PDFs”. In: *The European Physical Journal C* 75.5 (May 2015), p. 204. ISSN: 1434-6052. DOI: 10.1140/epjc/s10052-015-3397-6. URL: <https://doi.org/10.1140/epjc/s10052-015-3397-6> (cit. on p. 26).
- [3] Georges Aad et al. “Measurements of the Higgs boson production and decay rates and constraints on its couplings from a combined ATLAS and CMS analysis of the LHC pp collision data at $\sqrt{s} = 7$ and 8 TeV”. In: *JHEP* 08 (2016), p. 045. DOI: 10.1007/JHEP08(2016)045. arXiv: 1606.02266 [hep-ex] (cit. on pp. 29–32).

- [4] Matthias Schlaffer et al. “Boosted Higgs Shapes”. In: *Eur. Phys. J. C* 74.10 (2014), p. 3120. DOI: 10.1140/epjc/s10052-014-3120-z. arXiv: 1405.4295 [hep-ph] (cit. on p. 33).
- [5] Christophe Grojean et al. “Very boosted Higgs in gluon fusion”. In: *JHEP* 05 (2014), p. 022. DOI: 10.1007/JHEP05(2014)022. arXiv: 1312.3317 [hep-ph] (cit. on p. 33).
- [6] S. Dawson, I. M. Lewis, and Mao Zeng. “Usefulness of effective field theory for boosted Higgs production”. In: *Phys. Rev. D* 91 (2015), p. 074012. DOI: 10.1103/PhysRevD.91.074012. arXiv: 1501.04103 [hep-ph] (cit. on p. 33).
- [7] Morad Aaboud et al. “Search for light resonances decaying to boosted quark pairs and produced in association with a photon or a jet in proton-proton collisions at $\sqrt{s} = 13$ TeV with the ATLAS detector”. In: *Phys. Lett. B* 788 (2019), pp. 316–335. DOI: 10.1016/j.physletb.2018.09.062. arXiv: 1801.08769 [hep-ex] (cit. on p. 33).
- [8] Lyndon Evans and Philip Bryant. “LHC Machine”. In: *JINST* 3 (2008), S08001. DOI: 10.1088/1748-0221/3/08/S08001 (cit. on p. 36).
- [9] Chris Llewellyn Smith. “Genesis of the Large Hadron Collider”. In: *Phil. Trans. Roy. Soc. Lond. A* 373.2032 (2014), p. 20140037. DOI: 10.1098/rsta.2014.0037 (cit. on p. 36).

- [10] ATLAS Collaboration. “The ATLAS Experiment at the CERN Large Hadron Collider”. In: *JINST* 3 (2008), S08003. DOI: 10.1088/1748-0221/3/08/S08003 (cit. on pp. 47, 49, 55–63).
- [11] Giordon Holtsberg Stark. “The search for supersymmetry in hadronic final states using boosted object reconstruction”. Presented 26 Apr 2018. May 2018. URL: <https://cds.cern.ch/record/2317296> (cit. on pp. 51, 52).
- [12] Karolos Potamianos. *The upgraded Pixel detector and the commissioning of the Inner Detector tracking of the ATLAS experiment for Run-2 at the Large Hadron Collider*. Tech. rep. ATL-PHYS-PROC-2016-104. 15 pages, EPS-HEP 2015 Proceedings. Geneva: CERN, Aug. 2016. URL: <https://cds.cern.ch/record/2209070> (cit. on p. 53).
- [13] *ATLAS inner detector: Technical Design Report, 1*. Technical Design Report ATLAS. Geneva: CERN, 1997. URL: <http://cds.cern.ch/record/331063> (cit. on p. 53).
- [14] S Haywood et al. *ATLAS inner detector: Technical Design Report, 2*. Technical Design Report ATLAS. Geneva: CERN, 1997. URL: <https://cds.cern.ch/record/331064> (cit. on p. 53).
- [15] B. Abbott et al. “Production and integration of the ATLAS Insertable B-Layer”. In: *JINST* 13 (2018), T05008. DOI: 10.1088/1748-0221/13/05/T05008. arXiv: 1803.00844 [physics.ins-det] (cit. on p. 54).

- 994 [16] Christian Wolfgang Fabjan and F Gianotti. “Calorimetry for Particle Physics”.
995 In: *Rev. Mod. Phys.* 75.CERN-EP-2003-075 (Oct. 2003), 1243–1286. 96 p. DOI:
996 10.1103/RevModPhys.75.1243. URL: <https://cds.cern.ch/record/692252>
997 (cit. on p. 58).
- 998 [17] Keith Hamilton, Paolo Nason, and Giulia Zanderighi. “Finite quark-mass effects
999 in the NNLOPS POWHEG+MiNLO Higgs generator”. In: *Journal of High Energy*
1000 *Physics* 2015.5 (May 2015), p. 140. ISSN: 1029-8479. DOI: 10.1007/JHEP05(2015)
1001 140. URL: [https://doi.org/10.1007/JHEP05\(2015\)140](https://doi.org/10.1007/JHEP05(2015)140) (cit. on p. 67).
- 1002 [18] Keith Hamilton et al. “Merging H/W/Z + 0 and 1 jet at NLO with no merging
1003 scale: a path to parton shower + NNLO matching”. In: *JHEP* 05 (2013), p. 082.
1004 DOI: 10.1007/JHEP05(2013)082. arXiv: 1212.4504 [hep-ph] (cit. on p. 67).

1005 **Appendix A**

1006 **Hadronic Vqq Sherpa Studies**

1007 Ancillary material should be put in appendices, which appear after the bibliography.